

1 **Biocompatible Rhamnolipid Self-Assemblies with pH-Responsive Antimicrobial Activity**

2

3 *Parth Kadakia¹, Jules Valentin¹, Linda Hong¹, Samuel Watts¹, Owais Abdul Hameed^{1,2},*

4 *Michael Walch², Stefan Salentinig^{1*}*

5

6 ¹Department of Chemistry, University of Fribourg, Chemin du Musée 9, 1700 Fribourg,

7 Switzerland

8

9 ²Anatomy Unit, Department of Oncology, Microbiology and Immunology, Faculty of Science

10 and Medicine, University of Fribourg, Fribourg, Switzerland

11

12 *Corresponding author: Stefan Salentinig, email: stefan.salentinig@unifr.ch, Tel: +41 26 300

13 8794

14

15

1 **Keywords**

2 Antibacterial nanomaterials, pH-triggered self-assembly, rhamnolipids, SAXS, amphiphilic
3 lipids.

4

5 **Abstract**

6 There is an urgent need for alternative antimicrobial materials due to the growing challenge of
7 bacteria becoming resistant to conventional antibiotics. This study demonstrates the creation of
8 a biocompatible pH-switchable antimicrobial material by combining bacteria-derived
9 rhamnolipids (RL) and food-grade glycerol monooleate (GMO). The integration of RL into
10 dispersed GMO particles, with an inverse-type liquid crystalline cubic structure in the core,
11 leads to colloiddally stable supramolecular materials. The composition and pH-triggered
12 structural transformations are studied with small-angle X-ray scattering, cryogenic transmission
13 electron microscopy, and dynamic light scattering. The composition-structure-activity
14 relationship is analyzed and optimized to target bacteria at acidic of acute wounds. The new
15 RL/GMO dispersions reduce *Staphylococcus aureus* populations by 7-log after 24 h of
16 treatment with 64 $\mu\text{g mL}^{-1}$ of RL and prevent biofilm formation at pH = 5.0, but have no activity
17 at pH = 7.0. Additionally, the system is active against methicillin-resistant *S. aureus* (MRSA)
18 with MIC = 128 $\mu\text{g mL}^{-1}$ at pH 5.0. No activity was found against several Gram-negative
19 bacteria at pH 5.0 and 7.0.

20 The results provide a fundamental understanding of lipid self-assembly and the design of lipid-
21 based biomaterials, which can further guide the development of alternative bio-based solutions
22 to combat bacteria.

23

24

25

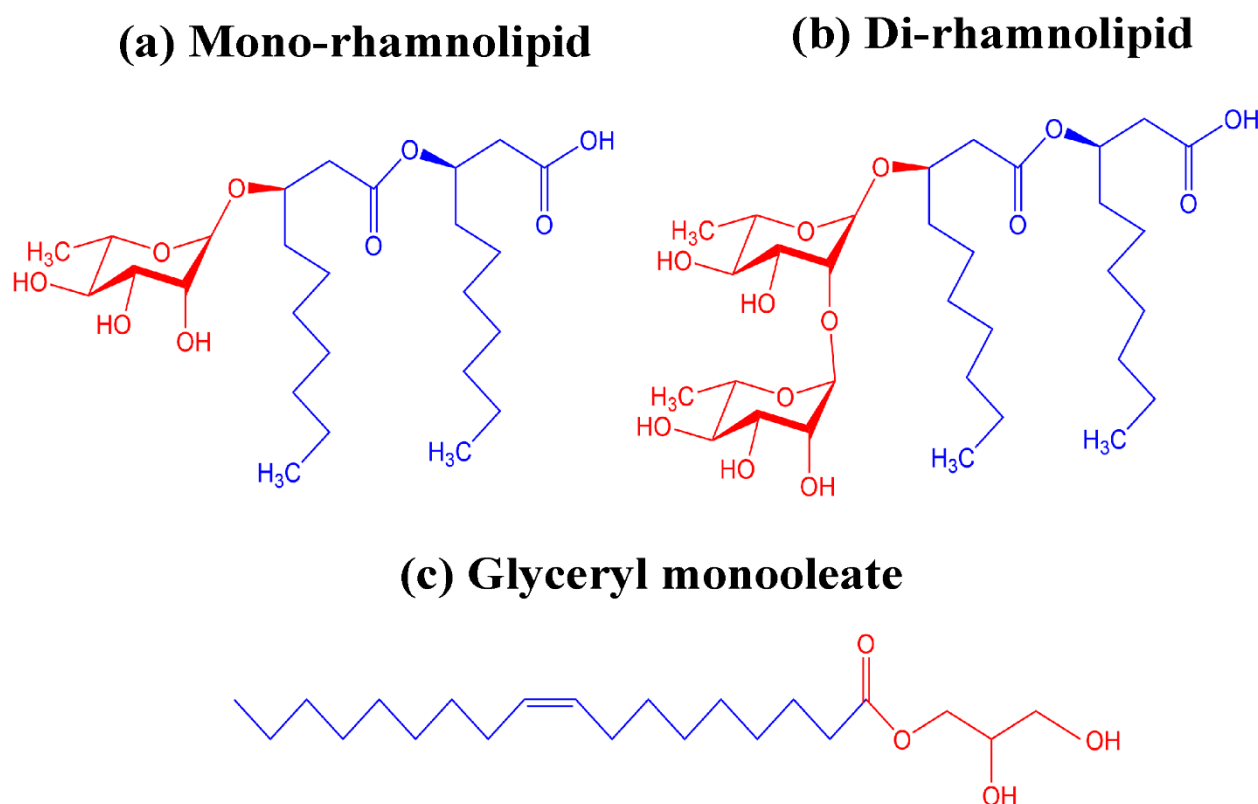
1 **1. Introduction**

2 The increasing prevalence of bacterial resistance to traditional antibiotics has become a primary
3 global concern.^[1] Hence, exploring and developing innovative strategies to combat bacteria is
4 urgently needed. Lipid-based antimicrobial nanomaterials emerged as promising candidates for
5 this purpose.^[2] The nanomaterials' size, shape, and surface charge are crucial in determining
6 their therapeutic efficacy against bacteria.^[2b, 3] They can be engineered to possess multimodal
7 bactericidal mechanisms, making them less susceptible to bacterial resistance and enabling
8 them to circumvent the resistance mechanisms developed against conventional antibiotics.^[2a, 4]
9 Stimuli-responsive antimicrobial biomaterials that target bacteria-infected sites can be
10 engineered from selected amphiphilic lipids and antimicrobial agents, such as antimicrobial
11 peptides.^[5] Notably, pH fluctuations are a stimulus of high biological relevance, showing
12 abnormal changes in pathological conditions such inflammation and bacterial infections.^[6] The
13 pH found in acute wounds, cystic fibrosis, abscesses, and osteomyelitis exhibit an acidic pH
14 environment (pH < 5.5) compared to normal tissues (pH 7.2-7.4).^[7] The pH of infected sites
15 can decrease from the accumulation of acidic by-products generated by bacterial metabolic
16 processes.^[8] Furthermore, bacterial biofilms, characterized as bacterial communities embedded
17 in a self-produced matrix, can harbor an acidic microenvironment within their core.^[9] Acidic
18 pH conditions found in these conditions can reduce the antimicrobial activity of certain
19 antibiotics and the immune system.^[6a, 10] Therefore, developing effective antimicrobial
20 nanomaterials is crucial for treating severe bacterial infections in an acidic pH environment.
21 Challenges in the further application of antimicrobial peptides are, for instance, their resource-
22 intensive synthesis and limited stability in biological environments.^[11] Hence, antimicrobial
23 agents that are widely available, cheap, and stable in biological environments are crucial for
24 further developing effective pH-triggered antimicrobials. In this context, bacteria-derived
25 rhamnolipids (RLs) are promising candidates.

1 RLs are a class of amphiphilic glycolipids produced naturally by *Pseudomonas aeruginosa* that
2 exhibit antibacterial activity against multiple Gram-positive pathogens.^[12] They are
3 biodegradable surfactants with a molecular structure consisting of one or two polar hydrophilic
4 rhamnose moieties linked to a short non-polar hydrophobic fatty acid chain containing a β -
5 hydroxyalkanote (**Figure 1a & 1b**).^[12b] The protonation/deprotonation state of the carboxyl
6 group in RLs can render them pH-responsive surfactants with a significant effect on their self-
7 assembly behavior, which can be understood by the critical packing parameter (CPP) model.^[13]
8 The CPP is defined as $v/(l_c a_0)$ with v being the hydrophobic chain volume, l_c the hydrophobic
9 chain length and a_0 the effective head-group area of the surfactant at the interface.^[13] Molecules
10 with a $CPP \leq 0.33$ form spherical micelles, while those exceeding up to 0.5 form elongated
11 micelles. Between CPP 0.5 and 1, flexible bilayers or vesicles form, with planar bilayers
12 dominating at a CPP near 1. Inverted structures (spherical, cylindrical and planar) emerge when
13 the CPP surpasses 1.^[13] Previous studies have reported the self-assembly of RLs in water into
14 various colloidal structures, such as lamellar phase and micelles, in the presence of electrolytes,
15 additives, and model lipid membranes.^[14]

16 The colloidal instability of RL-based nanomaterials at $pH < 6.0$ presents a challenge in
17 combating bacteria in acidic conditions.^[15] We hypothesized that RLs could be combined with
18 glyceryl monooleate (GMO) to form lipid nanomaterials to overcome this challenge. GMO is
19 a food-grade amphiphilic lipid that self-assembles into inverse bicontinuous cubic structures in
20 excess water.^[16] The molecular structure of GMO consists of a hydrophilic hydroxyl head group
21 attached to an unsaturated hydrophobic alkyl chain (**Figure 1c**).^[17] The pH-responsive
22 surfactant properties of RL could further transform GMO colloids into novel functional
23 antimicrobial nanomaterials. A detailed understanding of the RL/GMO self-assembly is crucial
24 for identifying the most suitable nanostructures regarding antibacterial activity,
25 biocompatibility, and stability at the relevant pH values of the infection site. Developing such
26 a novel therapeutic system will provide unique solutions for the current unmet clinical demands,

1 ultimately leading to the development of effective treatments for bacterial infections. This study
2 reports on designing RL/GMO-based lipid self-assemblies as an antimicrobial nanomaterial
3 with detailed pH-triggered modulation of the colloidal features and their biological activity.
4 The main goal of the current study is to (i) systematically characterize the self-assembly of RL
5 with GMO upon variations in pH and composition, and (ii) optimize the antimicrobial activity
6 and biocompatibility of the nanostructures. Small-angle X-ray scattering (SAXS), cryogenic
7 transmission electron microscopy (cryo-TEM), multi-angle dynamic light scattering (multi-
8 angle DLS), and zeta-potential measurements were used to investigate the nanostructure,
9 morphology, charge, and stability of the self-assembled structures at different pH. *In vitro*,
10 biological assays were performed to evaluate the antimicrobial activity of the nano self-
11 assemblies and their cytotoxicity against human dermal fibroblast (HDF) cells.



12 **Figure 1.** Molecular structures of (a) mono-rhamnolipid (mono-RL), (b) di-rhamnolipid (di-
13 RL), and (c) glyceryl monooleate (GMO). Hydrophilic and hydrophobic parts are highlighted
14 in red and blue color, respectively.

15

1 **2. Results and Discussion**

2 **2.1 Characterization of pH-responsive RL self-assembly in excess water**

3 The structure of F127-stabilized RL dispersions was studied using SAXS and cryo-TEM at pH
4 values ranging from 6.0 to 9.0. Pluronic F127, a triblock copolymer, is a commonly used
5 stabilizer for lipid-based particles for drug delivery applications.^[18] Below pH 6.0, aggregation
6 occurred 30 minutes after dispersion (see Figure S1 in the Supporting Information).
7 Consequently, the samples below pH 6.0 were not subjected to further analysis.

8 The SAXS curves of RL presented an approximate $q^{-2.5}$ decay of the $I(q)$ at low q values ($q <$
9 0.14 nm^{-1}) and a broad correlation peak between $q = 0.8 \text{ nm}^{-1}$ and 4.0 nm^{-1} at pH values between
10 6.0 and 9.0 (**Figure 2a**). The observed features suggest the presence of bilayer-like structures,
11 possibly vesicles, with the broad correlation peak likely corresponding to the variation in excess
12 electron densities within the bilayer's thickness region.^[19]

13 The SAXS data were further analyzed with the indirect Fourier transformation (IFT) method
14 that resulted in the pair distance distribution function $p(r)$ which is the real space
15 representation of the $I(q)$, allowing a direct determination of the size and shape of the scattering
16 objects.^[20] The overall size of RL appears beyond the resolution limit of the SAXS set-up of

17 $\frac{\pi}{q_{min}} \approx 62.8 \text{ nm}$. Since the IFT method requires a finite maximum distance, a cut-off value of

18 100 nm was chosen based on the results from cryo-TEM in **Figure 2** to truncate the $p(r)$
19 mathematically. The experimental SAXS data for the RL structures at pH 7.0 and the best
20 possible fit calculated with the IFT method are shown in **Figure S2a** (Supporting Information).

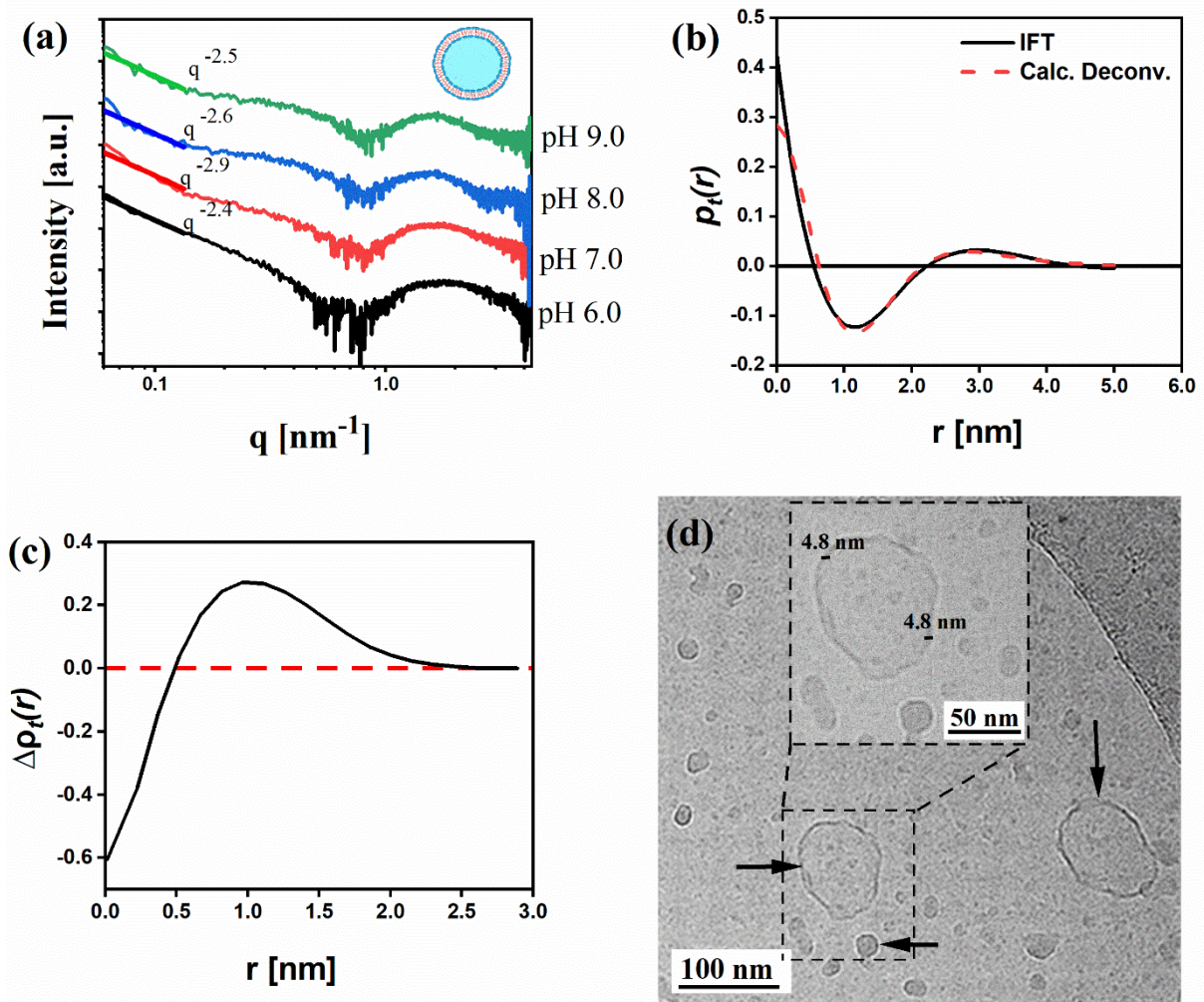
21 The shape of the $p(r)$ for the RL structures presented in **Figure S2b** is characteristic of vesicles:

22 The oscillations at $r < 10 \text{ nm}$ correspond to the variations in the excess electron density within
23 the bilayer region of the vesicles.^[21] The bilayer thickness of the RL vesicles was further

24 analyzed by calculating the thickness pair-distance distribution function, $p_t(r)$, from
25 the $I(q)$.^[22] The bilayer thickness, deduced from $p_t(r) = 0$, is at r around 5.0 nm (**Figure 2b**),

26 which agrees with the bilayer thickness of 4.8 nm as observed in the cryo-TEM in **Figure 2d**.

1 Deconvolution of the $p_t(r)$ using a convolution square-root operation led to the excess electron
 2 density distribution profile, $\Delta\rho_t(r)$, within the bilayer, as shown in **Figure 2c**. The half-bilayer
 3 thickness of RL is 2.6 nm, and the negative- and positive excess electron density relative to the
 4 PBS corresponds to the alkyl chain of RL and the rhamnose and carboxyl head group, including
 5 counter-ions. Cryo-TEM analysis of the RL dispersion at pH 7.0 confirmed the presence of
 6 vesicles of various sizes and shapes, mostly below 100 nm (**Figure 2d**).



7 **Figure 2.** Colloidal structures in the RL-water system. (a) SAXS curves of RL between pH 6.0-
 8 9.0, (b) Thickness pair distance distribution function $p_t(r)$ of the bilayer (black line) and
 9 corresponding fit (dashed red line) calculated by deconvolution of the $p_t(r)$ using a
 10 convolution square-root operation for RL at pH 7.0, (c) Excess electron density profile for the
 11 half-bilayer, relative to water, calculated from deconvolution of the $p_t(r)$ for RL at pH 7.0, and

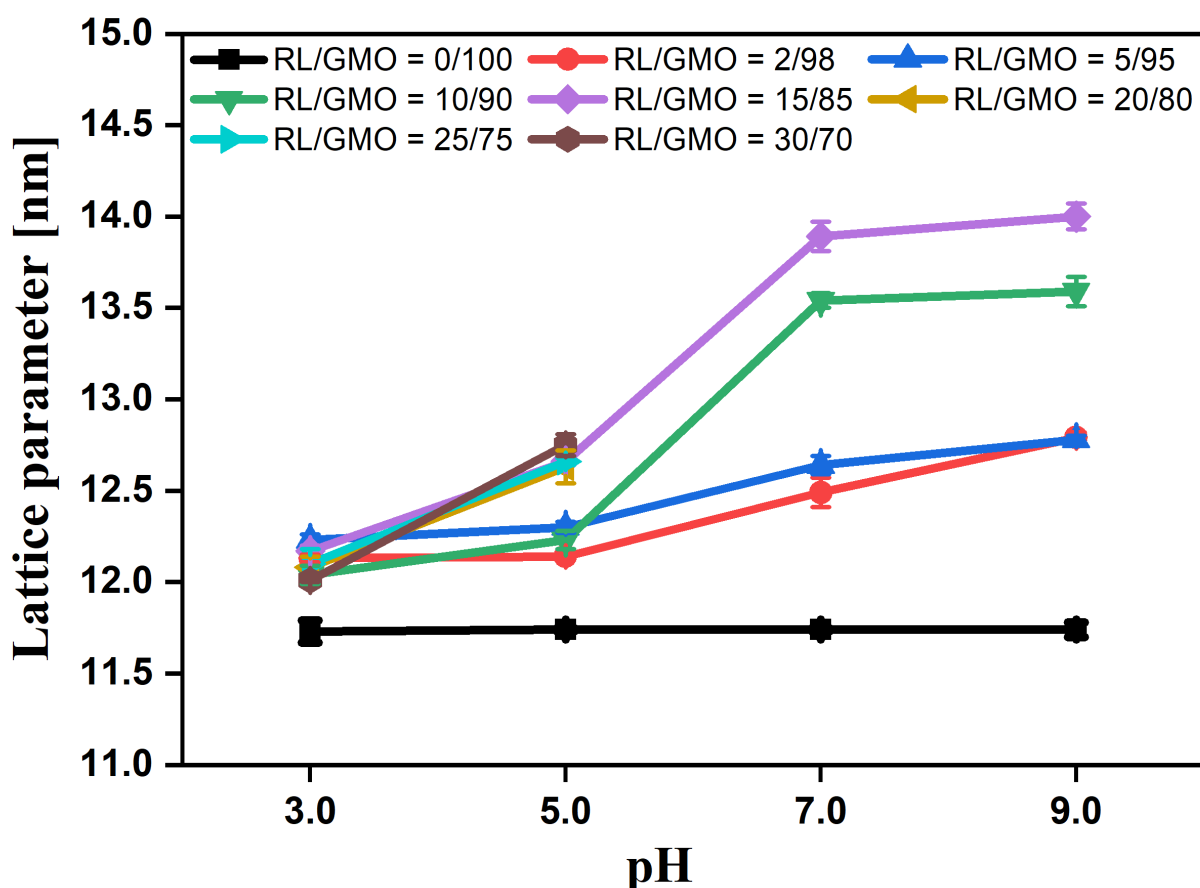
1 (d) representative cryo-TEM image of RL in PBS at pH 7.0 are dominated by nanoobjects of
2 various sizes, mostly below 100 nm.

3

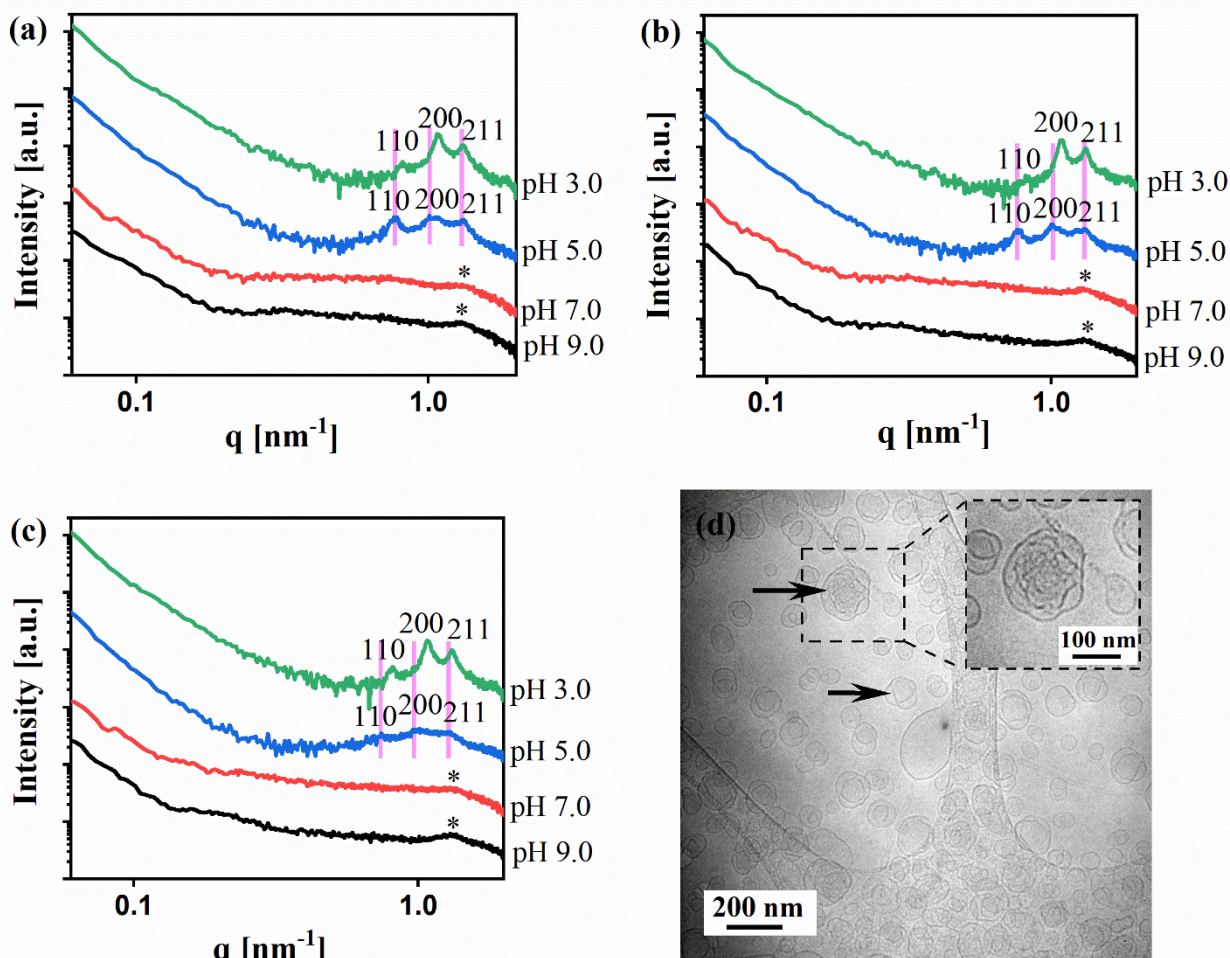
4 **2.2 Characterization of pH-driven RL/GMO self-assembly in water**

5 Contrary to the RL-water system, the RL/GMO system was discovered to form stable
6 dispersions for at least 2 months, even below pH 6.0 (Figure S3, Supporting Information). The
7 composition- and pH-triggered self-assembly of F127-stabilized RL/GMO colloids between pH
8 3.0-9.0 was determined. The SAXS data of the GMO cubosomes in the absence of RL between
9 pH 3.0-9.0 showed the presence of three Bragg peaks corresponding to the 110, 200, and 211
10 *hkl* reflections of the inverse bicontinuous cubic *Im3m* structure in agreement with previous
11 reports (Figure S4, Supporting Information).^[23] The calculated lattice parameter, a_{Im3m} , was
12 11.7 ± 0.1 nm at all the studied pH values, as found previously (**Figure 3**).^[16d, 24]

13 Upon addition of RL to GMO at RL/GMO = 2/98, 5/95, 10/90, and 15/85 w/w, the three Bragg
14 reflections of the *Im3m*-type cubic structure with a relative *q*-spacing of $\sqrt{2} : \sqrt{4} : \sqrt{6}$ remained
15 between pH 3.0-9.0 (Figure S4, Supporting Information). However, a shift of the peaks to lower
16 *q*-values is observed upon increasing the pH and RL content, which is characteristic of swelling
17 of the *Im3m* cubic structure. The respective lattice parameter, a_{Im3m} , calculated from these
18 reflections increased from 12.0 ± 0.1 nm at pH 3.0 to 14.0 ± 0.1 nm at pH 9.0 (**Figure 3**). The
19 individual lattice parameters are reported in Table S1 (Supporting Information).



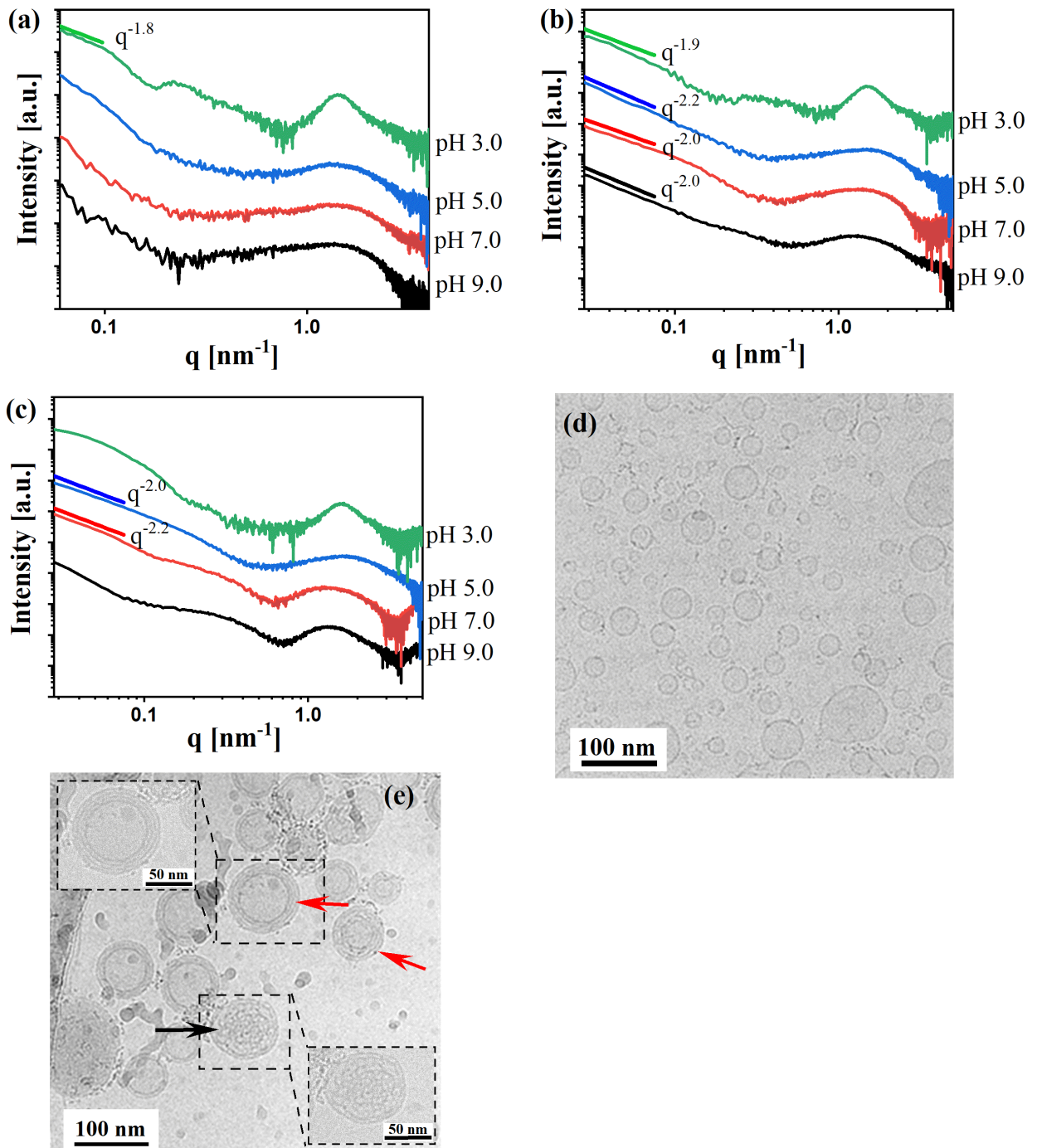
1 **Figure 3.** The change of a_{Im3m} with pH for different RL/GMO ratios between pH 3.0 and 9.0.
2
3 Increasing the RL content to RL/GMO = 20/80, 25/75, and 30/70 w/w, the $Im3m$ type cubic
4 structure dominated between pH 3.0-5.0 (**Figures 4a, 4b & 4c**). The Bragg reflections also
5 shifted to lower q values, and the peak intensity decreased upon increasing the pH, owing to
6 the swelling of the $Im3m$ type cubic structure and the formation of coexisting structures. The
7 calculated a_{Im3m} changed from 12.0 ± 0.1 nm at pH 3.0 to 12.7 ± 0.1 nm at pH 5.0 (**Figure 3**
8 **and Table S1**). At pH > 5.0, the Bragg peaks of the $Im3m$ structure are not visible anymore. A
9 broad correlation peak with a maximum at q around 1.3 nm^{-1} appeared for RL/GMO = 20/80 to
10 30/70 w/w (**Figures 4a, 4b & 4c**), which indicated the formation of a highly disordered cubic
11 phase, also denoted as the L3 sponge phase.^[25] The cryo-TEM investigation of the dispersion
12 at RL/GMO = 20/80 w/w sample at pH 7.0 confirmed the presence of dispersed particles with
13 the internal sponge phase (**Figure 4d**).



1 **Figure 4.** SAXS curves of (a) RL/GMO = 20/80, (b) RL/GMO = 25/75, and (c) RL/GMO =
 2 30/70 w/w dispersions between pH 3.0-9.0. The pink line is drawn for visual guidance
 3 representing the shift of the Bragg peaks in the SAXS curves. A broad correlation peak with a
 4 maximum at q around 1.3 nm^{-1} (indexed with *) can be observed between pH 7.0-9.0 indicating
 5 a sponge phase. (d) Representative cryo-TEM image of RL/GMO (20/80 w/w) sample at pH
 6 7.0 showing sponge-like particles coexisting with vesicles.

7
 8 At elevated RL/GMO = 50/50, 70/30, and 90/10 w/w, the SAXS curves between pH 5.0-9.0
 9 demonstrated a broad correlation peak between $q = 0.5 \text{ nm}^{-1}$ and 4.0 nm^{-1} with an
 10 approximate $q^{-2.2}$ decay of the $I(q)$ at low q values (**Figures 5a, 5b & 5c**). These features
 11 indicate the formation of vesicles.^[19] The cryo-TEM image of the sample (RL/GMO = 50/50
 12 w/w) at pH 7.0 confirms the presence of vesicles of various sizes, mostly below 100 nm (**Figure**

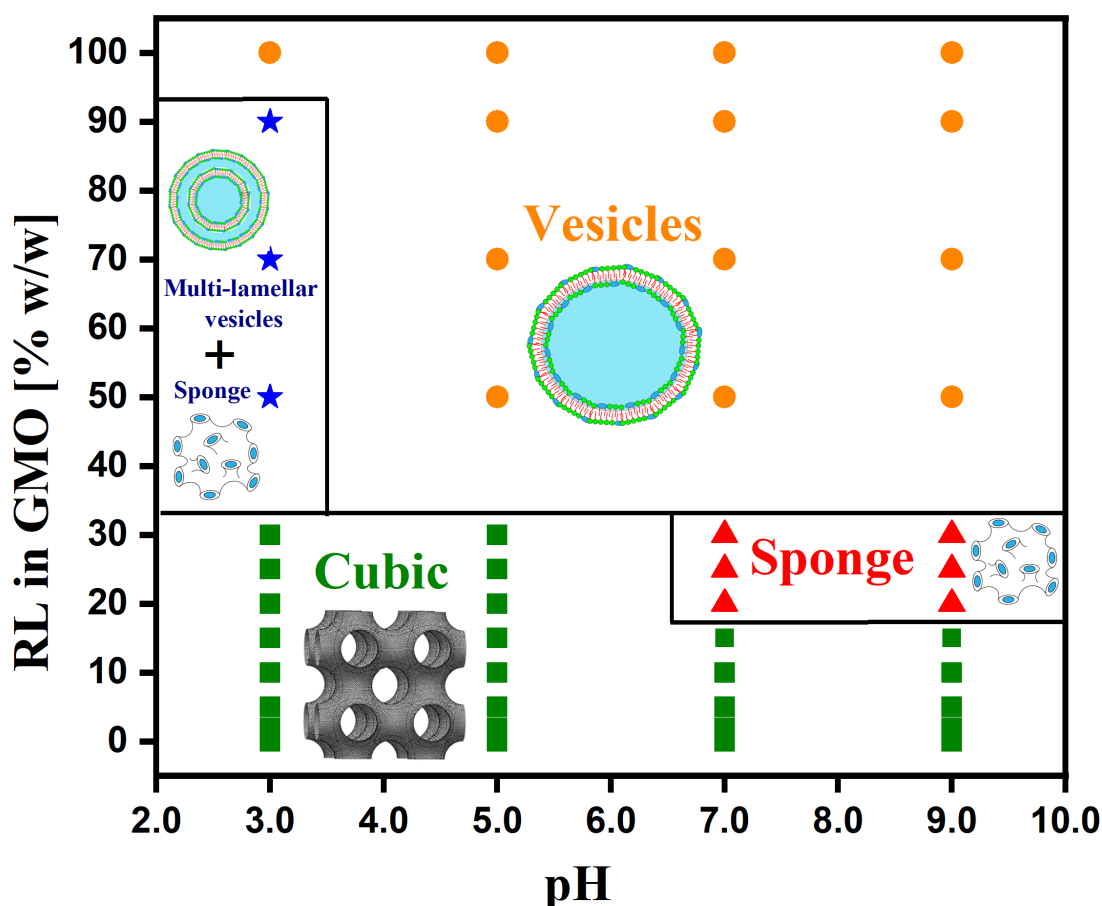
1 **5d)**. At pH 3.0, the SAXS curves at high q value showed a broad correlation peak with a
2 maximum of around 1.4 nm^{-1} , which may be attributed to the scattering of sponge structures.^[25]
3 At low q values, another broad correlation peak between $q = 0.18 \text{ nm}^{-1}$ to 0.3 nm^{-1} was seen
4 along with an approximate $q^{-1.9}$ decay of the $I(q)$ (**Figures 5a, 5b & 5c**). These features most
5 likely represent small multi-lamellar vesicles with a structure factor peak corresponding to a
6 real-space dimension of $\frac{2\pi}{q} \approx 25 \text{ nm}$.^[20b] Cryo-TEM on this sample (50/50 w/w at pH 3.0)
7 confirmed the findings from SAXS, showing multi-lamellar vesicles coexisting with sponge-
8 like particles and small nanoobjects, mostly corresponding to the 20 nm size range obtained
9 from the structure factor peak. (**Figure 5e**).



1 **Figure 5.** SAXS curves of (a) RL/GMO = 50/50, (b) RL/GMO = 75/25, (c) RL/GMO = 90/10
 2 w/w dispersions between pH 3.0-9.0. (d) Cryo-TEM image of RL/GMO (50/50 w/w) dispersion
 3 at pH 7.0 showing vesicles. (e) Cryo-TEM image of RL/GMO (50/50 w/w) sample at pH 3.0.
 4 Red and black arrows indicate multi-lamellar vesicles, and sponge structures, respectively.

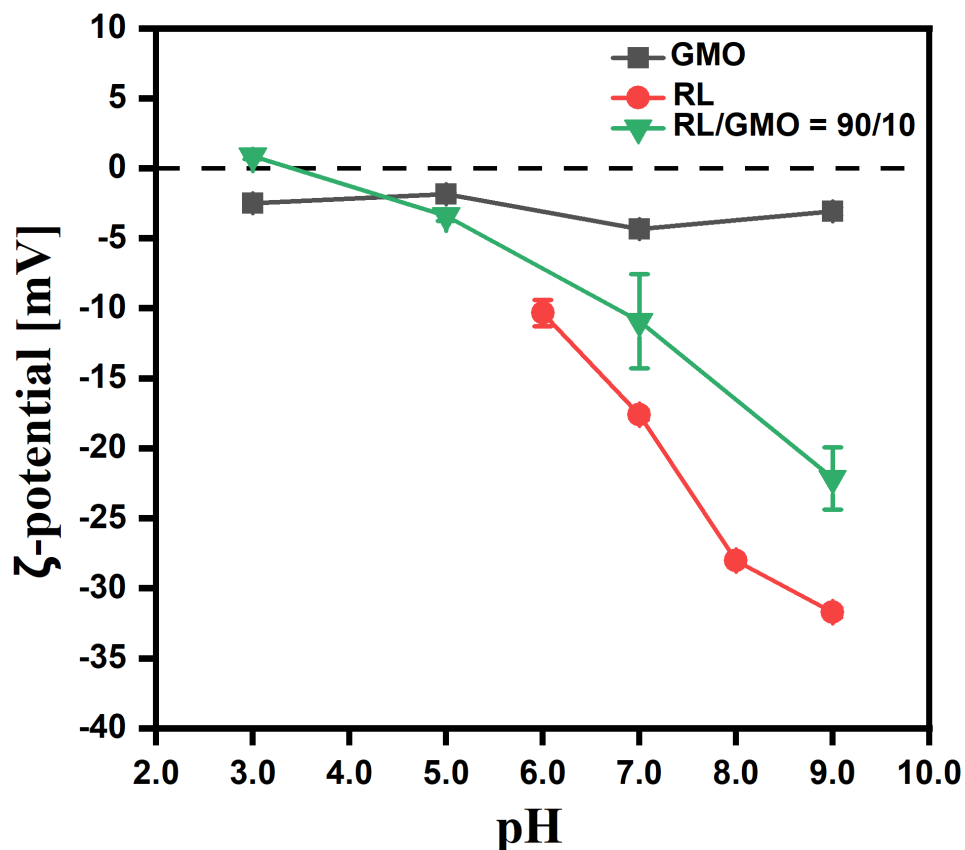
5

1 A phase diagram of different RL/GMO combinations was constructed based on the above
2 SAXS and cryo-TEM analysis (**Figure 6**). Regarding the critical packing parameter (CPP)
3 model,^[13] the RL molecules at the RL/GMO-water interface increased the effective headgroup
4 area of the surfactants at the lipid-water interface. Increasing the pH leads to deprotonation of
5 the carboxyl group of RL [pK_a of RL was reported to be 5.6].^[14c] Charge repulsions among the
6 negatively charged carboxyl groups of RL at pH values above 5.6 ($pH > pK_a$) further increase
7 the effective headgroup area. For example, the cubic structures dominated at all the pH values
8 up to RL/GMO = 15/85 w/w (**Figure 6**). Upon increasing the RL content to RL/GMO = 30/70
9 w/w, the effective headgroup area increased at $pH > 5.0$ and the formation of a sponge phase
10 (**Figure 6**). Such a structural alteration was attributed to the deprotonation of RL's carboxyl
11 head-groups and electrostatic repulsions among them at the lipid-water interface. At RL content
12 $> 30\%$ (concerning GMO), the effective headgroup area increased further, causing the CPP to
13 reach unity and favoring the formation of lamellar structures, for instance, in the form of
14 vesicles, between pH 3.0-9.0 (**Figure 6**).



1 **Figure 6.** Phase diagram showing different self-assemblies of RL/GMO combination upon
2 varying RL content (concerning GMO) and pH. The self-assembled structures formed in the
3 phase diagram were interchangeable upon pH circulation between pH 3.0-9.0. Each point on
4 the phase diagram represents a SAXS measurement in combination with cryo-TEM analysis.
5 The lines between phases are for visual guidance and do not indicate sharp phase boundaries.
6
7 To further analyze the pH-triggered protonation behavior of the RLs, ζ -potential measurements
8 were performed (**Figure 7**). The ζ -potential value of F127-stabilized GMO dispersion in PBS
9 ranged from $-2.5 \text{ mV} \pm 0.1$ to $-4.4 \text{ mV} \pm 0.2$ between pH 3.0-9.0, in agreement with a previous
10 report.^[5a] For RL dispersions, the ζ -potential values changed from $-10.4 \text{ mV} \pm 0.1$ at pH 6.0 to
11 $-31.7 \text{ mV} \pm 0.4$ at pH 9.0, owing to the deprotonation of the RL carboxyl group at $\text{pH} > pK_a$
12 [pK_a of RL = 5.6].^[14c] Similarly, in RL/GMO (90/10 w/w) dispersion, the ζ -potential values
13 decreased from $0.9 \text{ mV} \pm 0.2$ at pH 3.0 to $-22.2 \text{ mV} \pm 2.2$ at pH 9.0. Thus, the ζ -potential

1 analysis agrees with the results from the SAXS study, confirming our hypothesis that charge
2 repulsions at the lipid-water interface of the self-assembled structures mostly trigger structural
3 transformations.

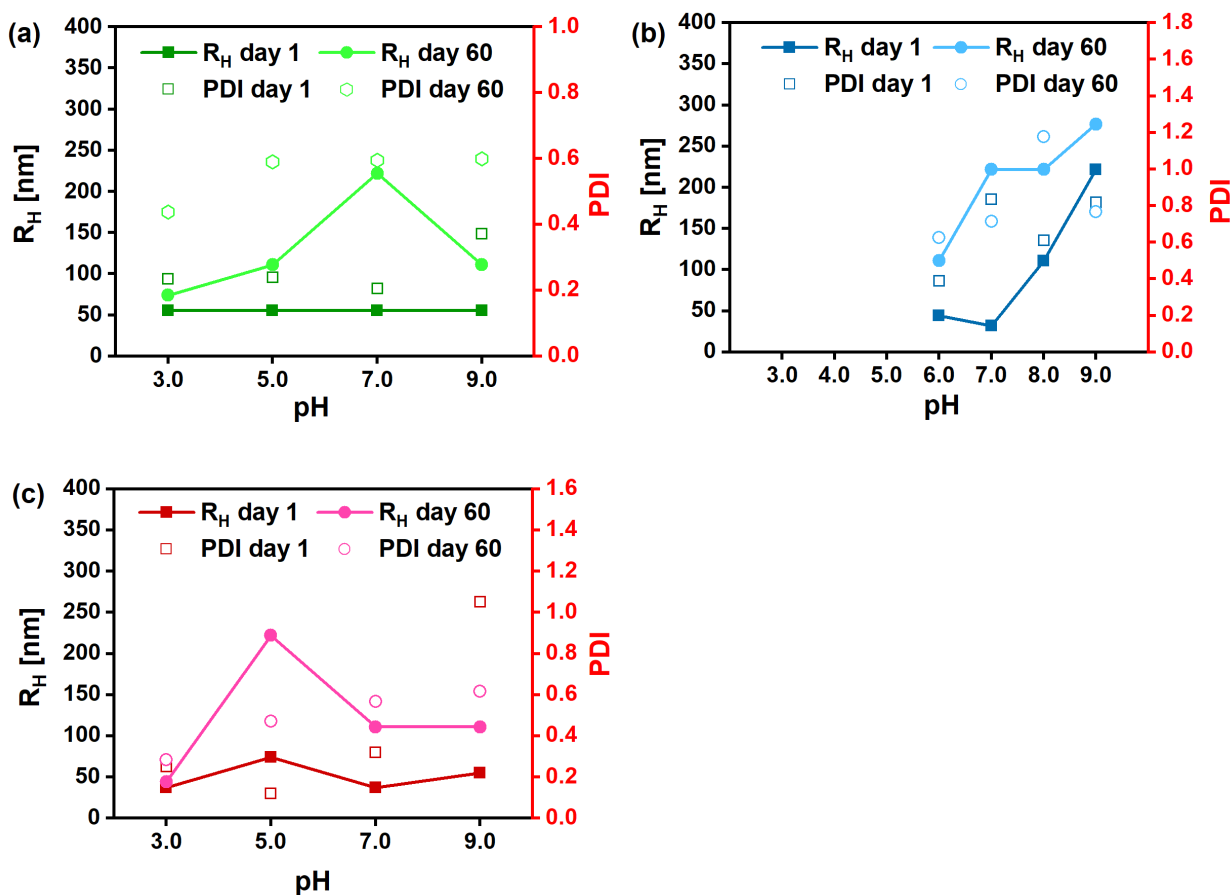


4 **Figure 7.** ζ -potential values of GMO, RL, and RL/GMO (90/10 w/w) dispersions between pH
5 3.0-9.0. The ζ -potential of RL dispersion could not be measured at pH < 6.0 due to its instability
6 at acidic pH and subsequent aggregation.

7
8 Notably, the RL/GMO (90/10 w/w) dispersion yielded similar ζ -potential values to those of the
9 GMO dispersion at pH levels below 7.0. The reduction in the ζ -potential values observed in the
10 RL/GMO mixture at acidic pH can be attributed to the protonation of the carboxyl group in the
11 RL molecule. Contrary to pure RL dispersions, the RL/GMO combinations remained
12 colloidally stable at pH < 6.0 (Figure S3, Supporting Information), indicating that the presence
13 of GMO had a stabilizing effect that prevented aggregation even in the presence of F127 in the
14 pure RL colloids.

1 Multi-angle DLS was used to characterize the dispersions' particle size and colloidal stability
 2 between pH 3.0 and 9.0. The apparent hydrodynamic radius, and PDI were analyzed at various
 3 scattering angles between 39 and 124° on day 1 and day 60 (see Table S2 & Figure S5,
 4 Supporting Information). The corresponding DLS intensity autocorrelation functions are shown
 5 in Figures S6-S8 (Supporting Information).

6 During day 1, the F127-stabilized GMO dispersion had an R_H of 55 nm that remained constant
 7 at pH 3.0-9.0 (PDI = 0.23-0.37) (**Figure 8a**). The RL dispersion had an R_H ranging from 44 to
 8 222 nm between pH 6.0-9.0 (PDI = 0.39-0.82) (**Figure 8b**). In RL/GMO combination (90/10
 9 w/w), the R_H value ranged from 37 to 55 nm between pH 3.0-9.0 (PDI = 0.25-1.05) (**Figure**
 10 **8c**). These values were considerably lower than those of the dispersions of the individual
 11 components (GMO and RL).



12 **Figure 8.** R_H and PDI values as a function of pH from multi-angle DLS for (a) GMO, (b) RL,
 13 and (c) RL/GMO (90/10 w/w) dispersions on day 1 and day 60, respectively. Day 1 refers to

1 measurements carried out immediately after sample preparation. The R_H of RL dispersion
2 could not be measured at $\text{pH} < 6.0$ due to their colloidal instability.

3

4 After 60 days, the dispersions were again analyzed using DLS. The R_H and PDI values of all
5 the dispersions increased between $\text{pH} 3.0\text{-}9.0$. For the GMO dispersion, the R_H increased to 74
6 nm at $\text{pH} 3.0$ (PDI = 0.44) and to 111 nm at $\text{pH} 9.0$ (PDI = 0.60) when comparing day 1 and
7 day 60 (**Figure 8a**). For the RL vesicles, the R_H on day 60 increased to 111 nm (PDI = 0.63) at
8 $\text{pH} 6.0$ and to 277 nm (PDI = 0.77) at $\text{pH} 9.0$ (**Figure 8b**) compared to day 1. For the RL/GMO
9 dispersion at a ratio of 90/10 w/w, the DLS analysis showed that the R_H value increased to 44
10 nm (PDI = 0.28) at $\text{pH} 3.0$ and to 111 nm (PDI = 0.62) at $\text{pH} 9.0$ when comparing day 1 and
11 day 60 (**Figure 8c**). While there was an increase in particle size for all three dispersions, the
12 increase in R_H for the RL/GMO = 90/10 w/w formulation was smaller compared to the GMO
13 cubosomes and the RL alone. In sum, DLS analysis showed that the RL/GMO combination had
14 a stabilizing effect, which prevented significant particle size growth even after 60 days and
15 prevented instability in the formulations. The results further suggested the RL/GMO = 90/10
16 w/w system as a promising candidate for further development as an antimicrobial nanomaterial.

17

18 **2.3 Antibacterial and Cytotoxicity Study**

19 Following the CLSI guidelines,^[26] the antibacterial properties of the RL/GMO formulations
20 were investigated *in vitro* by measuring the MIC and MBC against the *S. aureus* strain (Gram-
21 positive) at $\text{pH} 5.0$ and 7.0 . The MIC and MBC values are reported in **Table 1**, and the log
22 reductions of *S. aureus* after 24 h treatment are shown in **Figure 9**.

23 The RL/GMO = 90/10 vesicles had a MIC and MBC of $64 \mu\text{g mL}^{-1}$ against *S. aureus* at $\text{pH} 5.0$,
24 resulting in a >7 -log reduction after 24 h treatment (**Table 1 and Figure 9**). Moreover, after
25 two months of storage, RL/GMO vesicles were still as active as on day 1 against *S. aureus* with
26 an MBC of $64 \mu\text{g mL}^{-1}$ at $\text{pH} 5.0$ (Figure S9, Supporting Information). The similar MIC and

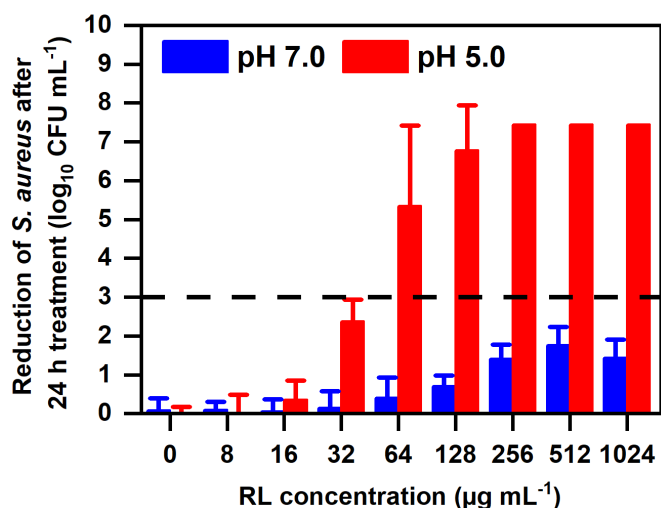
1 MBC values suggest that RL/GMO vesicles are bactericidal at pH 5.0, actively killing bacteria
 2 instead of preventing bacterial growth.^[27] The same antibacterial activity was found for pure
 3 RL vesicles (**Table 1 and Figure S10**). However, the colloidal instability of RLs at 1wt% at
 4 pH < 6.0 (see discussion above) makes them unsuitable for medical applications. Adding 10
 5 wt% GMO to RL significantly improved the stability of RL without impacting its antimicrobial
 6 activity.

7 Similar to a previous study using RLs,^[12a] RL/GMO structures had no bactericidal activity
 8 against *S. aureus* at pH 7.0 with up to 1024 µg mL⁻¹ of RL (**Figure 9**). We hypothesized that
 9 the pH-dependent bactericidal activity of RL might be related to modifications in their surface
 10 charge. As shown in **Figure 7**, RLs in RL/GMO combination are negatively charged at pH 7.0,
 11 which likely increased repulsions between RLs and the anionic bacterial membrane and thus
 12 reduced interactions. In contrast, lowering the pH to 5.0 neutralized the charge of the RL/GMO
 13 self-assemblies, favoring their interactions with the bacterial cell membrane that induced the
 14 killing of the bacteria. However, further work is needed to decipher the bactericidal mechanisms
 15 of the formulations.

16
 17 **Table 1.** MIC and MBC values of GMO, RL, and RL/GMO (90/10) at pH 5.0 against *S. aureus*
 18 and MRSA.

Formulation	MIC [µg mL ⁻¹]		MBC [µg mL ⁻¹]
	<i>S. aureus</i>	MRSA	<i>S. aureus</i>
GMO	*	*	469
RL	64	128	64
RL/GMO (90/10)	64	128	64

19 *The MIC readout was impossible due to the dispersed GMO's high optical density.



1 **Figure 9.** Antibacterial activity of RL/GMO (90/10 w/w) formulations against *S. aureus* at pH
 2 5.0 and 7.0, respectively. The dashed line represents the 3-log reduction threshold, indicating
 3 the bactericidal activity (n = 3).

4

5 Further experiments were conducted to assess the impact of RL/GMO (90/10 w/w) formulations
 6 on the formation and stability of biofilms. Biofilms have significant clinical relevance,
 7 associated with most persistent infections in humans and exhibiting high resistance to antibiotic
 8 treatments.^[9a, 28] The ability of the formulation to prevent biofilm formation (Figure S11a,
 9 Supporting Information) and to eradicate established biofilms (Figure S11b, Supporting
 10 Information) was assessed against *S. aureus* at pH 5.0. The RL/GMO = 90/10 w/w system
 11 inhibited *S. aureus* biofilm formation by >50% with 32 µg mL⁻¹ of RL (Figure S11a, Supporting
 12 Information). Pure RL vesicles, used as a positive control, showed similar inhibition against
 13 biofilm formation. In contrast, both RL/GMO = 90/10 w/w and RL alone could not eradicate
 14 established biofilms but promoted their growth in a concentration-dependent manner (Figure
 15 S11b, Supporting Information). Hence, these results highlight that the RL/GMO system can
 16 effectively inhibit *S. aureus* biofilm formation in an acidic environment of pH 5.0, while further
 17 optimization is required to eradicate established biofilms.

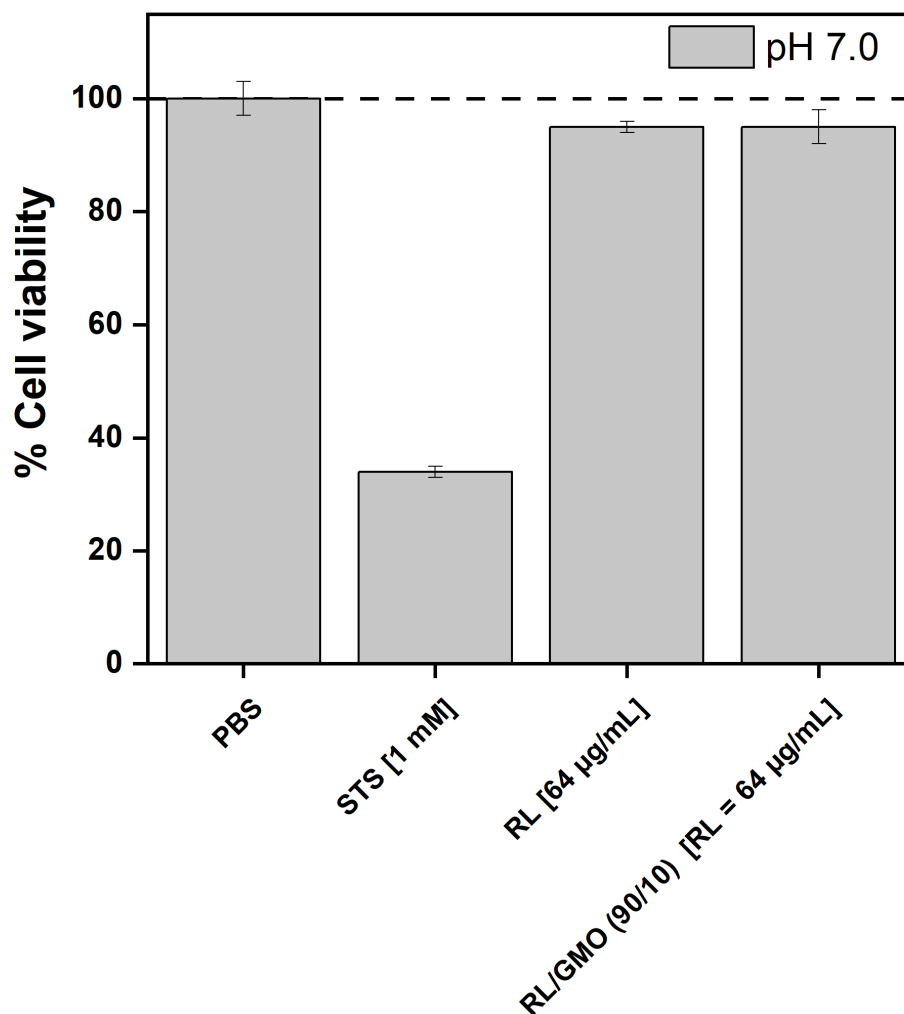
18 The antibacterial activity of the formulation was also assessed against other bacterial strains in
 19 solution at pH 5.0 and 7.0: methicillin-resistant *S. aureus* (MRSA), *Listeria monocytogenes* (*L.*

1 *monocytogenes*), *Escherichia coli* (*E. coli*), and *Salmonella typhimurium* (*S. typhimurium*). A
2 MIC of 128 $\mu\text{g mL}^{-1}$ RL in the formulation was found against MRSA at pH 5.0 while inactive
3 at pH 7.0 (**Table 1** and **Figure S12**). In contrast, no antibacterial activity up to RL = 1024 μg
4 mL^{-1} was found against *L. monocytogenes*, *S. typhimurium*, and *E. coli* at pH 5.0 and 7.0 (**Table**
5 **S3** and **Figures S13-S15**, Supporting Information). The observed inactivity of the RL/GMO
6 formulation and pure RL against the Gram positive *L. monocytogenes* strain somehow contrasts
7 with a previous study evaluating the effect of RL.^[12a] This disparity may be attributed to
8 differing susceptibilities among various *L. monocytogenes* strains.^[29] The resistance of Gram-
9 negative bacteria to RL has been attributed to the presence of the outer membrane.^[12a]

10 The antibacterial activity of various RL/GMO ratios at 70/30, 50/50, 20/80, 5/95, and 0/100
11 was further investigated. Pure GMO dispersions (cubosomes) as a negative control showed an
12 MBC of 469 $\mu\text{g mL}^{-1}$ against *S. aureus* at pH 5.0 (**Table 1** & Figure S10, Supporting
13 Information). In contrast, no bactericidal activity was observed at pH 7.0 with up to 30 mg mL^{-1}
14 of GMO. As acidic pH reduces the protective barrier function of the bacterial cell wall,^[30]
15 high concentrations of the amphiphilic GMO molecules may compromise membrane stability
16 in a low pH environment. In RL/GMO mixtures, the antibacterial activity against *S. aureus* at
17 pH 5.0 decreased as the GMO content increased (Figure S16, Supporting Information). The
18 increased GMO content with the formation of sponge and cubic structures likely hinders the
19 interaction between the RL molecules and the bacteria membrane. None of the tested ratios
20 exhibited any activity against *S. aureus* at pH 7.0 (Figure S16, Supporting Information). Hence,
21 GMO at concentrations above 10wt% does not synergize with RL, and the ratio RL/GMO =
22 90/10 shows the highest antibacterial activity.

23 The cytotoxicity of RL/GMO (90/10 w/w) and RL was assessed using human dermal fibroblasts
24 (HDF). HDF are essential in maintaining the physical integrity of connective tissue and
25 producing and remodeling the extracellular matrix.^[31] The MTS assay evaluated HDF viability
26 *in vitro* after exposure to RL and RL/GMO = 90/10 w/w. The results were normalized to the

1 cell viability in PBS at pH 7.0. RL and RL/GMO = 90/10 w/w combination exhibited cell
2 viability of $95 \pm 1\%$ and $95 \pm 3\%$ after 24 h at pH 7.0 (Figure 10).
3 The assay could not be performed at pH 5.0 as the HDF do not survive at $\text{pH} < 6.0$ after 24 h.^[32]
4 Consistent with previous reports,^[32] the cell viability decreased to $28 \pm 2\%$ in PBS, $31 \pm 1\%$ for
5 RL, and $27 \pm 2\%$ for RL/GMO (90/10 w/w) dispersions. The results indicated that RL and
6 RL/GMO (90/10 w/w) formulations are non-toxic and compatible with HDF at pH 7.0.
7 Therefore, the RL/GMO (90/10) combination is an ideal and stable formulation for effective
8 and safe multiple uses for combating Gram-positive bacteria in acidic conditions, such as those
9 found in bacteria-infected locations and in acidic food products.



10 **Figure 10.** Viability of HDF after 24 h treatment with RL [$64 \mu\text{g mL}^{-1}$] and RL/GMO (90/10
11 w/w) ratio [RL concentration = $64 \mu\text{g mL}^{-1}$ and GMO concentration = $7 \mu\text{g mL}^{-1}$] at pH 7.0.

- 1 PBS and STS [final concentration = 1mM] were used as the negative and positive controls,
- 2 respectively (n = 3).
- 3

1 3. Conclusion

2 This study demonstrates the design of antimicrobial nanomaterials based on bacteria-derived
3 RL and food-grade GMO that is active at pH 5.0. While RL alone phase separates in water
4 within minutes at this pH, the GMO self-assemblies solubilize RL into colloiddally stable
5 supramolecular structures. SAXS and cryo-TEM show that the size and shape of the RL/GMO
6 nanomaterials are highly composition and pH-dependent. Increasing the RL concentration in
7 GMO, the *Im3m* type cubic structure swells and eventually transforms into sponge-like
8 nanoparticles and vesicles. Increasing the pH in the RL/GMO assemblies favors the formation
9 of vesicles. The pH-triggered colloidal transformations result from the protonation or
10 deprotonation of the pH-sensitive headgroup of the RLs and are found reversible upon pH
11 circulation. A decrease in the ζ -potential values from +0.9 mV to -22.2 mV is observed in
12 RL/GMO upon an increase in pH from 3.0 to 9.0. The RL/GMO (90/10 w/w) vesicles show
13 significant bactericidal and antibiofilm formation activity against the Gram-positive pathogen
14 *S. aureus* at pH 5.0, but are inactive at pH 7.0. Interestingly, the RL/GMO nanomaterial is found
15 active against MRSA at pH 5.0, but inactive against Gram-negative *E. coli* and *S. typhimurium*,
16 presumably due to the presence of the outer membrane as compared to *S. aureus*. Cytotoxicity
17 studies show that RL/GMO (90/10 w/w) combination is non-toxic against HDF at pH 7.0. The
18 results demonstrate a novel pH-responsive antimicrobial biomaterial that selectively targets
19 Gram-positive bacteria such as *S. aureus* and MRSA at pH values below 6.0. This system can
20 be of interest for various antimicrobial applications in food and health science fields.

21

1 **4. Experimental Section**

2 *Materials:* Rhamnolipid [90% pure, R90] was purchased in solid form from Agae Technologies,
3 Oregon, U.S.A. It is a mixture of mono-rhamnolipids ($C_{26}H_{48}O_9$, molecular weight = 504 g mol⁻¹)
4 and di-rhamnolipids ($C_{32}H_{58}O_{13}$, molecular weight = 650 g mol⁻¹) at a ratio of 3:2. Dimodan[®]
5 MO 90/D Kosher, distilled glyceryl monooleate (GMO, $C_{21}H_{40}O_4$, molecular weight = 356.5 g
6 mol⁻¹), was supplied by DANISCO, Denmark. It contains a minimum of 90% total
7 monoglyceride and a maximum of 1% free glycerol. Pluronic F127 was acquired from Sigma,
8 St Louis, MO, U.S.A. Phosphate buffered saline (PBS, 1×, pH 7.4) consisted of 137 mM NaCl
9 (Acros Organics, 99.5% purity, Denmark), 2.7 mM KCl (Carl Roth, Karlsruhe, Germany), 10
10 mM $Na_2HPO_4 \cdot 2H_2O$ (Sigma-Aldrich, Steinheim, Germany), and 1.8 mM KH_2PO_4 (Sigma-
11 Aldrich, Steinheim, Germany). NaOH pellets (> 99% purity) were procured from Sigma-
12 Aldrich, and a ~ 37% HCl stock solution (analytical reagent grade) was obtained from Fischer
13 Scientific, U.S.A. 1M NaOH and 1M HCl solutions adjusted the pH of the buffer and the
14 samples. Ultra-pure water (resistivity > 18MΩcm) was used from Sartorius arium Mini Lab
15 Water Systems (Göttingen, Germany) for the preparation of the buffer. All chemicals were used
16 as received without any additional purification.

17 *Sample Preparation:* RL was weighed in a glass vial and dispersed in PBS buffer (pH 7.4)
18 containing Pluronic F127 (0.1% w/w) to achieve a 1 wt% RL in buffer solution. The system
19 was homogenized using ultrasonication using a tip sonicator [Lab500 NextGen Ultrasonic
20 platform (SinapTec, Lezennes, France)] at 25% amplitude [Maximum power = 500 root mean
21 square watts (RMSW)] for 2 min in pulse mode (3 s pulse, 3 s break). The samples were
22 adjusted to defined pH values between pH 3.0 and 9.0 using 1M HCl or 1M NaOH solution.
23 The same protocol was used to prepare GMO (1% w/w) dispersions in PBS containing Pluronic
24 F127 (0.1% w/w).

25 To prepare RL/GMO combinations (final lipid concentration at 1% w/w), RL and GMO were
26 first weighed in the defined mass ratios ranging between RL/GMO = 2/98 and 90/10 into a glass

1 vial. Then PBS buffer (pH 7.4) containing Pluronic F127 (0.1% w/w) was added to them and
2 sonicated as described above. Finally, all the different RL/GMO samples were pH adjusted to
3 defined values between pH 3.0 and 9.0 using 1M HCl or 1M NaOH solution. All the prepared
4 samples were equilibrated at 25 °C for at least 12 h before further experiments.

5 *Methods: Small Angle X-ray Scattering (SAXS):* Small angle X-ray scattering measurements
6 were carried out at the Austrian SAXS beamline at Elettra (Trieste, Italy).^[33] The photon energy
7 was 8 keV (wavelength, $\lambda = 0.154$ nm), and the sample-to-detector distance was 1752.99 mm,
8 yielding a q -range of 0.05 to 4.2 nm⁻¹. The magnitude of the scattering vector, q , was calculated
9 using equation (1):

$$10 \quad q = \frac{4\pi}{\lambda} \sin\left(\frac{\theta}{2}\right) \quad (1)$$

11 where θ is the scattering angle. The size of the beam was 0.4×1.4 μm . The scattering images
12 were recorded by a 2D Pilatus3 1 M Detector System (Dectris Ltd, Baden-Dättwil, Switzerland)
13 with a total area of 168.7×179.4 mm² and pixel size of 172×172 μm^2 . The scattering images
14 were converted to a 1D pattern with the SAXSDOG software.^[34] Quartz capillary was used to
15 load the samples and placed in line with the beam. Data was collected from four acquisitions
16 (15 s each) at 25 °C. The capillary was rinsed with water and ethanol after every sample
17 measurement and then dried with pressured air. The scattering replicates were compared to
18 identify any potential beam damage. The replicates were averaged since no beam damage could
19 be observed. The scattering of the PBS was measured separately and subtracted as background
20 from all samples.

21 *Analysis of SAXS Data:* The Bragg peaks in the SAXS curves were assigned to the space groups
22 for the liquid crystalline structures based on their hkl Miller indices.^[35] The cubic phases' lattice
23 parameter, a_{Im3m} , was calculated from the corresponding Bragg peak position, q_{hkl} , using
24 equation (2). The average and standard deviation were calculated from the visible peaks.

$$25 \quad a = \frac{2\pi}{q_{hkl}} \sqrt{h^2 + k^2 + l^2} \quad (2)$$

1 Vesicles were identified by their characteristic low- q power-law scattering with an around q^{-2}
2 dependence of the $I(q)$.^[19a] The Indirect Fourier Transformation (IFT) method was further used
3 for the model-free analysis of the scattering data for vesicles.^[20b] The pair-distance distribution
4 function $p(r)$ is calculated by the IFT method to gain information about the scattering objects'
5 size, shape, and morphology.^[20a] The $p(r)$ is obtained from the scattering intensity $I(q)$ by
6 using equation (3):

$$7 \quad I(q) = 4\pi \int_0^{\infty} p(r) \frac{\sin(qr)}{qr} dr \quad (3)$$

8 where $p(r)$ is given by $p(r) = r^2 \Delta\rho^2(r)$, where $\Delta\rho^2(r)$ represents the convolution square of
9 the excess electron density relative to the buffer, $\Delta\rho(r)$, averaged for all directions in space. To
10 extract $\Delta\rho(r)$ from $p(r)$, a deconvolution procedure is carried out with a prior assumption
11 about the symmetry of the system (spherical, lamellar, or cylindrical).^[36] Since the bilayer
12 thickness is very small than the vesicle diameter, the assumption of locally flat lamellar
13 structures is employed for evaluation and calculation of a thickness pair-distance distribution
14 function, $p_t(r)$.^[22] Deconvolution of the $p_t(r)$ results in the thickness contrast profile, $\Delta\rho_t(r)$,
15 which gives information about the excess electron density distribution within the bilayer.

16 *Cryogenic Transmission Electron Microscopy (cryo-TEM)*: For cryo-TEM analysis, 3.1 μl of
17 the sample at 1% w/w concentration was applied onto Quantifoil R2/1 300 mesh copper grids,
18 which were previously negatively glow-discharged at 25 mA for 30 s. Excess of the sample
19 was blotted away for 2 s and plunge-frozen in liquid ethane/propane mixture (continuously
20 cooled by liquid nitrogen) using Vitrobot Mark IV (ThermoFisher Scientific). The environmental
21 chamber was used at 100% humidity and 22 °C. Vitrified grids were screened in Titan Krios
22 (ThermoFischer Scientific) electron microscope in EFTEM mode (20eV slit width) using a
23 Gatan K2 camera. K2 integrated micrographs representing a cumulative dose of ~ 20 electrons
24 per \AA^2 were collected at approximately ~ 3 μm defocus and 1.4 \AA pixel size.

1 *Multi-angle Dynamic Light Scattering (DLS)*: Multi-angle DLS measurements were carried out
 2 with a light scattering goniometer (CGS-8F, ALV, Langen, Germany) and a solid-state laser
 3 (Coherent Verdi V5, 532 nm wavelength, max. power of 5W) with a single-mode fiber
 4 detection optics (OZ from GMP, Zürich, Switzerland), 8 fiber-optic detectors and ALV 7004
 5 correlators with fast expansion (ALV, Langen, Germany). The samples were measured at
 6 scattering angles ranging between 39 and 124° in 17° steps. Five accumulations with 10 s per
 7 sample was acquired. The temperature was set to 25 °C for all measurements. Samples were
 8 diluted at a 1:10 ratio with PBS to avoid multiple scattering, and pH was re-adjusted if necessary.
 9 To determine the apparent diffusion coefficient (D), the DLS autocorrelation functions were
 10 fitted using 2nd-order cumulant analysis.^[37] The average decay constant ($\bar{\Gamma}$) obtained from
 11 fitting the correlation functions using the cumulant analysis was plotted against q^2 and
 12 subjected to linear regression to determine the apparent translational diffusion (D):

$$\bar{\Gamma} = Dq^2 + c \quad (4)$$

14 where c represents the intercept. The refractive index used for PBS was 1.33. The
 15 hydrodynamic radius (R_H) was calculated from D using the Stokes-Einstein equation:

$$R_H = \frac{k_b T}{6\pi\eta D} \quad (5)$$

17 where k_b is the Boltzmann constant, T is the absolute temperature (298 K), η the solvent's
 18 viscosity (PBS, 1 mPa s). The PDI was determined from the second cumulant (μ_2):

$$PDI = \frac{\mu_2}{\bar{\Gamma}^2} \quad (6)$$

20 *Zeta-Potential*: Zeta-potential measurements were performed on a DelsaMax Pro Zeta Potential
 21 Dynamic Light Scattering Analyzer (Beckman Coulter, Indianapolis, USA). It employs
 22 Massively Parallel Phase Analysis Light Scattering (MP-PALS) to determine the
 23 electrophoretic mobility^[38] and calculates the zeta-potential via Smoluchowski's theory
 24 (equation 7):

$$\mu_e = \frac{\epsilon_r \epsilon_0 \zeta}{\eta} \quad (7)$$

1 where μ_e is the electrophoretic mobility, ϵ_r is the dielectric constant of the medium, ϵ_0 is the
2 permittivity of the vacuum, and ζ is the zeta-potential. All the samples were diluted at a 1:10
3 ratio with PBS and re-adjusted between pH 3.0-9.0 if necessary. All measurements were
4 performed at 25 °C.

5 *Antimicrobial Assay:* The antimicrobial activity of GMO, RL, and RL/GMO self-assemblies
6 was assessed against *S. aureus* ATCC 3555, MRSA (BAA 1720), *L. monocytogenes* ATCC
7 15313, *S. typhimurium* (SL1344) and *E. coli* ATCC 25922 following the Clinical and
8 Laboratory Standards Institute (CLSI) guidelines ^[26] and the broth microdilution protocol of
9 Wiegand *et al.*^[39] The different RL/GMO stocks were prepared in PBS containing F127 by
10 mixing 2048 $\mu\text{g mL}^{-1}$ of RL with 0, 228, 878, 2048, 8192, and 38912 $\mu\text{g mL}^{-1}$ of GMO for the
11 100/0, 90/10, 70/30, 50/50, 20/80, and 5/95 ratios, respectively. The ratio between lipids to
12 F127 was kept at 1:10. The stock solutions were UV-sterilized before use. Each stock solution
13 was twofold diluted in PBS at pH 5.0 and 7.0, and 50 μL of each dilution was dispatched in 96-
14 well plates. In parallel, *S. aureus*, MRSA, *S. typhimurium*, and *E. coli* overnight cultures were
15 grown in Mueller-Hinton Broth (non-cation-adjusted, MHB) and were used to prepare bacterial
16 suspensions at 1×10^6 CFU mL^{-1} in MHB 2 \times at pH 5.0 and 7.0. *L. monocytogenes* cultures
17 were grown overnight and prepared in brain heart infusion (BHI) media for the assay.
18 Subsequently, 50 μL of *S. aureus*, MRSA, *L. monocytogenes*, *S. typhimurium*, and *E. coli*
19 suspensions were mixed with 50 μL of RL/GMO serial dilutions at the corresponding pH value,
20 resulting in a final bacterial concentration of 5×10^5 CFU mL^{-1} and RL concentrations ranging
21 from 1024 to 8 $\mu\text{g mL}^{-1}$. The microtiter plates were then incubated at 37 °C for 24 h. The
22 minimum inhibitory concentration (MIC) values were determined by measuring the optical
23 density at 600 nm (OD_{600}). The minimum bactericidal concentration (MBC) values were
24 determined by diluting each well tenfold, spotting 10 μL of each dilution on MHB agar plates,
25 and CFU counting after overnight incubation at 37 °C. Following the CLSI guidelines, the MIC
26 is determined as the lowest concentration inhibiting the visible bacterial growth after 24 h

1 treatment.^[25] The MBC is the lowest concentration leading to > 99.9 % (>3-log) reduction of
2 the initial inoculum after 24 h treatment.^[25] The microbial log reduction is calculated as the
3 logarithmic difference between the CFU count after 24 h culture in the untreated and RL-treated
4 conditions. If not stated otherwise, the assay was done in triplicate with two technical repeats
5 per condition, and the two technical repeats were merged for the CFU counting.

6

7 *Biofilm Inhibition Assay*: The ability of RL/GMO = 90/10 dispersion to inhibit *S. aureus* biofilm
8 formation was assessed as previously described.^[40] Briefly, an overnight culture of *S. aureus*
9 grown in TSB media (100% of the manufacturer specifications, BD Bacto, Thermo Fischer
10 Scientific, Cat# DF0370-17-3) was used to prepare a bacterial suspension at 1×10^6 CFU mL⁻¹
11 into TSB media prepared at 20% of the original TSB concentration, supplemented with 2 mg
12 mL⁻¹ of glucose (D-(+)-Glucose, BioXtra, $\geq 99.5\%$, Sigma-Aldrich) and adjusted to pH 5.0.
13 50 μ L of the *S. aureus* suspension was dispatched in 96 well plates. In parallel, RL/GMO stocks
14 were prepared as previously described in PBS at 2X the final desired concentrations and
15 adjusted to pH 5.0. 50 μ L of the RL/GMO stock was added to the bacterial suspension, leading
16 to a final bacterial concentration of 5×10^5 CFU mL⁻¹, a media concentration of 10% TSB and
17 1 mg mL⁻¹ of glucose, and RL concentrations ranging from 1024 to 2 μ g mL⁻¹. The 96-well
18 plates were then incubated at 37 °C for 24 h under static conditions. After 24 h, the media was
19 removed, and the adhered biomass was washed thrice with 0.9% NaCl. The biofilm biomass
20 was stained with 0.1% crystal violet solution (CV, V5265, Sigma-Aldrich) for 20 min and
21 rinsed three times with 0.9% NaCl to remove unbound dye. The biofilm bound dye was
22 dissolved in 70% ethanol and quantified by OD₅₉₅ measurements. Biofilm formation inhibition
23 was calculated relative to the biofilm biomass grown without RL (defined as 100% biofilm)
24 and the sterility control (defined as 0% biofilm). The assay was performed in triplicates.

25

1 *Biofilm Eradication Assay:* The ability of RL/GMO dispersion to eliminate established *S.*
2 *aureus* biofilms was assessed as described previously.^[40] Briefly, biofilms were allowed to form
3 for 24 h at 37°C in 10% TSB media supplemented with 1 mg mL⁻¹ of glucose at pH 7. Following
4 incubation, the media was removed, and the adhered biofilm was rinsed thrice with 0.9% NaCl.
5 Next, 100 µL of RL/GMO dispersion prepared in PBS adjusted to pH 5.0 with RL
6 concentrations ranging from 1024 to 8 µg mL⁻¹ was applied to the biofilms for 24 h at 37°C
7 under static conditions. After 24 h treatment, the remaining biofilm biomass was quantified by
8 CV staining. Biofilm eradication was calculated relative to the remaining biofilm biomass in
9 the untreated conditions (100% biofilm) and the sterility control (0% biofilm). The assay was
10 performed in triplicates.

11 *Cytotoxicity Assay:* The cytotoxicity of RL (64 µg mL⁻¹) and RL/GMO = 90/10 w/w (RL
12 concentration = 64 µg mL⁻¹ and GMO concentration at 7 µg mL⁻¹) dispersions in PBS
13 containing F127 was assessed using the MTS assay (#ab197010, Abcam, Cambridge, UK) at
14 both pH 5.0 and 7.0 following the manufacturer's instructions. The ratio between lipids to F127
15 was maintained at 1:10. PBS and Staurosporine (STS) (final concentration = 1mM) were used
16 as negative and positive controls, respectively. Briefly, HDF cells (#106K-05a, Cell
17 Applications, Inc. U.S.A) were seeded at a concentration of 5 × 10³ per well in 96-well plates
18 in 100 µL of fibroblast growth medium (#116-500, Cell Applications, Inc. U.S.A). The cells
19 were cultured for 24 h at 37 °C and 5% CO₂ humidity before treatment. Following 24 h, the
20 fibroblast growth medium was replaced with PBS buffer (pH 5.0 and pH 7.0, respectively) and
21 100 µL of RL, and RL/GMO dispersions were added to the cells, which were then incubated at
22 37 °C and 5% CO₂ humidity for an additional 24 h. Subsequently, 20 µL of MTS reagent was
23 added to the cells to assess the cell viability. Following another 24 h incubation at 37 °C,
24 absorbance was measured at a wavelength of 490 nm using a spectrophotometer (Multiskan
25 SkyHigh, ThermoScientific, U.S.A). The assay was performed in triplicates, and cell viability
26 was calculated by repeating the above procedure without cells as the background.

1 **Supporting Information**

2 Supporting Information is available online or from the author.

3 **Acknowledgments**

4 The Swiss National Science Foundation funded this work through project no. 192051. The
5 authors thank the CERIC-ERIC Consortium for access to the Austrian SAXS beamline at the
6 Elettra Synchrotron (outstation of the Institute of Inorganic Chemistry, Graz University of
7 Technology) and Heinz Amenitsch for technical support. The authors further acknowledge the
8 Scientific Center for Optical and Electron Microscopy (ScopeM) of ETH Zürich for access to
9 the cryo-TEM and Miroslav Peterek for technical support. The authors are also grateful to Prof.
10 Michal Borkovec and the department of Chemistry, University of Geneva, for the generous
11 donation of the multi-angle DLS equipment.

12

13 **Conflict of Interest**

14 The authors declare no conflict of interest.

15

16 **Data Availability**

17 The data supporting this study's findings are available from the corresponding author upon
18 reasonable request.

19

20 **References**

- 21 [1] a)C. J. Murray, K. S. Ikuta, F. Sharara, L. Swetschinski, G. R. Aguilar, A. Gray, C.
22 Han, C. Bisignano, P. Rao, E. Wool, *The Lancet* **2022**, 399, 629; b)J. O'Neill, *Antimicrobial*
23 *resistance: tackling a crisis for the health and wealth of nations* **2014**, 2014; c)C. L. Ventola,
24 *Pharmacy and therapeutics* **2015**, 40, 277.
25 [2] a)J. M. V. Makabenta, A. Nabawy, C.-H. Li, S. Schmidt-Malan, R. Patel, V. M.
26 Rotello, *Nature Reviews Microbiology* **2021**, 19, 23; b)L.-S. Wang, A. Gupta, V. M. Rotello,
27 *ACS infectious diseases* **2016**, 2, 3.
28 [3] A. Gupta, R. F. Landis, V. M. Rotello, *F1000Research* **2016**, 5.
29 [4] R. Y. Pelgrift, A. J. Friedman, *Advanced drug delivery reviews* **2013**, 65, 1803.
30 [5] a)M. Gontsarik, M. T. Buhmann, A. Yaghmur, Q. Ren, K. Maniura-Weber, S.
31 Salentinig, *The Journal of Physical Chemistry Letters* **2016**, 7, 3482; b)M. Gontsarik, M.

1 Mohammadtaheri, A. Yaghmur, S. Salentinig, *Biomaterials science* **2018**, 6, 803; c)M.
2 Gontsarik, A. Yaghmur, Q. Ren, K. Maniura-Weber, S. Salentinig, *ACS applied materials &*
3 *interfaces* **2018**, 11, 2821; d)M. Zabara, B. Senturk, M. Gontsarik, Q. Ren, M. Rottmar, K.
4 Maniura - Weber, R. Mezzenga, S. Bolisetty, S. Salentinig, *Advanced Functional Materials*
5 **2019**, 29, 1904007.
6 [6] a)H.-P. Simmen, J. Blaser, *The American journal of surgery* **1993**, 166, 24; b)H. Ding,
7 P. Tan, S. Fu, X. Tian, H. Zhang, X. Ma, Z. Gu, K. Luo, *Journal of Controlled Release* **2022**,
8 348, 206.
9 [7] a)L. A. Schneider, A. Korber, S. Grabbe, J. Dissemond, *Archives of dermatological*
10 *research* **2007**, 298, 413; b)F. G. Costa, A. R. Horswill, *PLoS Pathogens* **2022**, 18, e1010512;
11 c)S. M. Kim, G. Zou, H. Kim, M. Kang, S. Ahn, H. Y. Heo, J.-S. Kim, K.-M. Lim, F. M.
12 Ausubel, E. Mylonakis, *Biomedicine & Pharmacotherapy* **2022**, 150, 112977; d)F. Rippke, E.
13 Berardesca, T. M. Weber, *pH of the Skin: Issues and Challenges* **2018**, 54, 87.
14 [8] a)A. F. Radovic-Moreno, T. K. Lu, V. A. Puscasu, C. J. Yoon, R. Langer, O. C.
15 Farokhzad, *ACS nano* **2012**, 6, 4279; b)Y. Gao, Q. Ma, *Smart Medicine* **2022**, 1, e20220012;
16 c)Y. Yang, X. Jiang, H. Lai, X. Zhang, *Journal of Functional Biomaterials* **2022**, 13, 173.
17 [9] a)H.-C. Flemming, J. Wingender, U. Szewzyk, P. Steinberg, S. A. Rice, S. Kjelleberg,
18 *Nature Reviews Microbiology* **2016**, 14, 563; b)D. S. Benoit, H. Koo, Vol. 11, *Future*
19 *Medicine*, 2016; c)S. Fulaz, D. Hiebner, C. H. Barros, H. Devlin, S. Vitale, L. Quinn, E.
20 Casey, *ACS applied materials & interfaces* **2019**, 11, 32679.
21 [10] a)A. Lardner, *Journal of leukocyte biology* **2001**, 69, 522; b)J. H. Yang, S. C. Bening,
22 J. J. Collins, *Current opinion in microbiology* **2017**, 39, 73; c)E. R. Ballou, G. M. Avelar, D.
23 S. Childers, J. Mackie, J. M. Bain, J. Wagener, S. L. Kastora, M. D. Panea, S. E. Hardison, L.
24 A. Walker, *Nature microbiology* **2016**, 2, 1.
25 [11] M.-D. Seo, H.-S. Won, J.-H. Kim, T. Mishig-Ochir, B.-J. Lee, *Molecules* **2012**, 17,
26 12276.
27 [12] a)J. de Freitas Ferreira, E. A. Vieira, M. Nitschke, *Food Research International* **2019**,
28 116, 737; b)A. M. Abdel-Mawgoud, F. Lépine, E. Déziel, *Applied microbiology and*
29 *biotechnology* **2010**, 86, 1323.
30 [13] a)J. Israelachvili, *Colloids and Surfaces A: Physicochemical and Engineering Aspects*
31 **1994**, 91, 1; b)O. Glatter, S. Salentinig, *Current opinion in colloid & interface science* **2020**,
32 49, 82.
33 [14] a)N. Baccile, C. Seyrig, A. Poirier, S. Alonso-de Castro, S. L. Roelants, S. Abel,
34 *Green Chemistry* **2021**, 23, 3842; b)Ş. Helvacı, S. Peker, G. Özdemir, *Colloids and Surfaces*
35 *B: Biointerfaces* **2004**, 35, 225; c)Y. Ishigami, Y. Gama, H. Nagahora, M. Yamaguchi, H.
36 Nakahara, T. Kamata, *Chemistry Letters* **1987**, 16, 763; d)J. T. Champion, J. C. Gilkey, H.
37 Lamparski, J. Retterer, R. M. Miller, *Journal of Colloid and Interface Science* **1995**, 170, 569;
38 e)K. H. Shin, K. W. Kim, J. Y. Kim, K. E. Lee, S. S. Han, *Journal of environmental quality*
39 **2008**, 37, 509; f)M. Chen, J. Penfold, R. Thomas, T. Smyth, A. Perfumo, R. Marchant, I.
40 Banat, P. Stevenson, A. Parry, I. Tucker, *Langmuir* **2010**, 26, 18281; g)B. Dahrazma, C. N.
41 Mulligan, M.-P. Nieh, *Journal of colloid and interface science* **2008**, 319, 590; h)E. Haba, A.
42 Pinazo, R. Pons, L. Pérez, A. Manresa, *Biochimica et Biophysica Acta (BBA)-Biomembranes*
43 **2014**, 1838, 776; i)H. G. Mortensen, J. K. Madsen, K. K. Andersen, T. Vosegaard, G. R.
44 Deen, D. E. Otzen, J. S. Pedersen, *Biophysical journal* **2017**, 113, 2621.
45 [15] a)R. B. Lovaglio, F. J. dos Santos, M. J. Junior, J. Contiero, *Colloids and Surfaces B:*
46 *Biointerfaces* **2011**, 85, 301; b)L. Bai, D. J. McClements, *Journal of colloid and interface*
47 *science* **2016**, 479, 71.
48 [16] a)M. E. Leser, L. Sagalowicz, M. Michel, H. J. Watzke, *Advances in colloid and*
49 *interface science* **2006**, 123, 125; b)T. Landh, *The journal of physical chemistry* **1994**, 98,
50 8453; c)J. Gustafsson, H. Ljusberg-Wahren, M. Almgren, K. Larsson, *Langmuir* **1996**, 12,

1 4611; d)J. Gustafsson, H. Ljusberg-Wahren, M. Almgren, K. Larsson, *Langmuir* **1997**, 13,
2 6964.
3 [17] R. Prajapati, M. Gontsarik, A. Yaghmur, S. Salentinig, *Langmuir* **2019**, 35, 7954.
4 [18] a)G. Popescu, J. Barauskas, T. Nylander, F. Tiberg, *Langmuir* **2007**, 23, 496; b)A. J.
5 Tilley, C. J. Drummond, B. J. Boyd, *Journal of colloid and interface science* **2013**, 392, 288;
6 c)J. Y. Chong, X. Mulet, L. J. Waddington, B. J. Boyd, C. J. Drummond, *Soft Matter* **2011**, 7,
7 4768.
8 [19] a)P. W. Schmidt, *Journal of Applied Crystallography* **1982**, 15, 567; b)S. Watts, M.
9 Ramstedt, S. Salentinig, *The Journal of Physical Chemistry Letters* **2021**, 12, 9557.
10 [20] a)J. Brunner-Popela, O. Glatter, *Journal of Applied Crystallography* **1997**, 30, 431;
11 b)O. Glatter, *Journal of Applied Crystallography* **1977**, 10, 415.
12 [21] a)R. V. Freire, Y. Pillco-Valencia, G. C. da Hora, M. Ramstedt, L. Sandblad, T. A.
13 Soares, S. Salentinig, *Journal of Colloid and Interface Science* **2021**, 596, 352; b)S.
14 Salentinig, L. Sagalowicz, M. E. Leser, C. Tedeschi, O. Glatter, *Soft Matter* **2011**, 7, 650.
15 [22] O. Glatter, *Journal of Applied Crystallography* **1980**, 13, 577.
16 [23] L. Hong, M. Gontsarik, H. Amenitsch, S. Salentinig, *Small* **2022**, 18, 2104211.
17 [24] M. Nakano, T. Teshigawara, A. Sugita, W. Leesajakul, A. Taniguchi, T. Kamo, H.
18 Matsuoka, T. Handa, *Langmuir* **2002**, 18, 9283.
19 [25] a)B. Angelov, A. Angelova, R. Mutafchieva, S. Lesieur, U. Vainio, V. M. Garamus,
20 G. V. Jensen, J. S. Pedersen, *Physical Chemistry Chemical Physics* **2011**, 13, 3073; b)D.
21 Anderson, H. Wennerstroem, U. Olsson, *The Journal of Physical Chemistry* **1989**, 93, 4243;
22 c)S. Engström, K. Alfons, M. Rasmusson, H. Ljusberg-Wahren, in *The Colloid Science of*
23 *Lipids*, Springer, 1998.
24 [26] N. C. f. C. L. Standards, A. L. Barry, *Methods for determining bactericidal activity of*
25 *antimicrobial agents: approved guideline*, Vol. 19, National Committee for Clinical
26 Laboratory Standards Wayne, PA, **1999**.
27 [27] J. L. Davis, *Equine internal medicine* **2018**, 4, 79.
28 [28] C. W. Hall, T.-F. Mah, *FEMS microbiology reviews* **2017**, 41, 276.
29 [29] L. Magalhães, M. Nitschke, *Food Control* **2013**, 29, 138.
30 [30] a)P. A. Lund, D. De Biase, O. Liran, O. Scheler, N. P. Mira, Z. Cetecioglu, E. N.
31 Fernández, S. Bover-Cid, R. Hall, M. Sauer, *Frontiers in microbiology* **2020**, 11, 556140;
32 b)E. A. Mueller, P. A. Levin, *MBio* **2020**, 11, e02456.
33 [31] Z. Zhu, J. Ding, Z. Ma, T. Iwashina, E. E. Tredget, *Wound Repair and Regeneration*
34 **2017**, 25, 377.
35 [32] C. R. Kruse, M. Singh, S. Targosinski, I. Sinha, J. A. Sørensen, E. Eriksson, K.
36 Nuutila, *Wound Repair and Regeneration* **2017**, 25, 260.
37 [33] H. Amenitsch, M. Rappolt, M. Kriechbaum, H. Mio, P. Laggner, S. Bernstorff,
38 *Journal of synchrotron radiation* **1998**, 5, 506.
39 [34] M. Burian, C. Meisenbichler, D. Naumenko, H. Amenitsch, *arXiv preprint*
40 *arXiv:2007.02022* **2020**.
41 [35] S. T. Hyde, *Handbook of applied surface and colloid chemistry* **2001**, 2, 299.
42 [36] O. Glatter, *Journal of Applied Crystallography* **1981**, 14, 101.
43 [37] B. J. Frisken, *Applied optics* **2001**, 40, 4087.
44 [38] J. F. Miller, K. Schätzel, B. Vincent, *Journal of colloid and interface science* **1991**,
45 143, 532.
46 [39] I. Wiegand, K. Hilpert, R. E. Hancock, *Nature protocols* **2008**, 3, 163.
47 [40] E. F. Haney, M. J. Trimble, J. T. Cheng, Q. Vallé, R. E. Hancock, *Biomolecules* **2018**,
48 8, 29.
49

1 **Table of contents**

2 This study presents a novel antimicrobial nanomaterial developed through the self-assembly of
3 rhamnolipids (RL) and glycerol monooleate (GMO). The nanomaterial undergoes pH-triggered
4 colloidal transformations, and RL/GMO in a 90/10 ratio provides colloiddally stable
5 antimicrobial nanomaterials. The nanomaterials effectively reduce *Staphylococcus aureus* and
6 methicillin-resistant *S. aureus* populations at pH 5.0 but are inactive at pH 7.0. They can also
7 inhibit *S. aureus* biofilm formation and are biocompatible with human dermal fibroblasts. This
8 study highlights the potential of the nanomaterial for various applications, providing a
9 foundation for alternative antimicrobial solutions to combat bacteria.

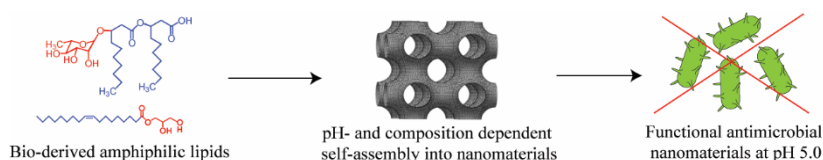
10

11 Parth Kadakia¹, Jules Valentin¹, Linda Hong¹, Samuel Watts¹, Owais Abdul Hameed^{1,2},
12 Michael Walch², Stefan Salentinig^{1*}

13

14 **Biocompatible Rhamnolipid Self-Assemblies with pH-Responsive Antimicrobial Activity**

15



16

17

18

1 Supporting Information

2

3 **Biocompatible Rhamnolipid Self-Assemblies with pH-Responsive Antimicrobial Activity**

4

5 *Parth Kadakia¹, Jules Valentin¹, Linda Hong¹, Samuel Watts¹, Owais Abdul Hameed^{1,2},*
6 *Michael Walch², Stefan Salentinig^{1*}*

7

8 ¹Department of Chemistry, University of Fribourg, Chemin du Musée 9, 1700 Fribourg,
9 Switzerland

10

11 ²Anatomy Unit, Department of Oncology, Microbiology and Immunology, Faculty of Science
12 and Medicine, University of Fribourg, Fribourg, Switzerland

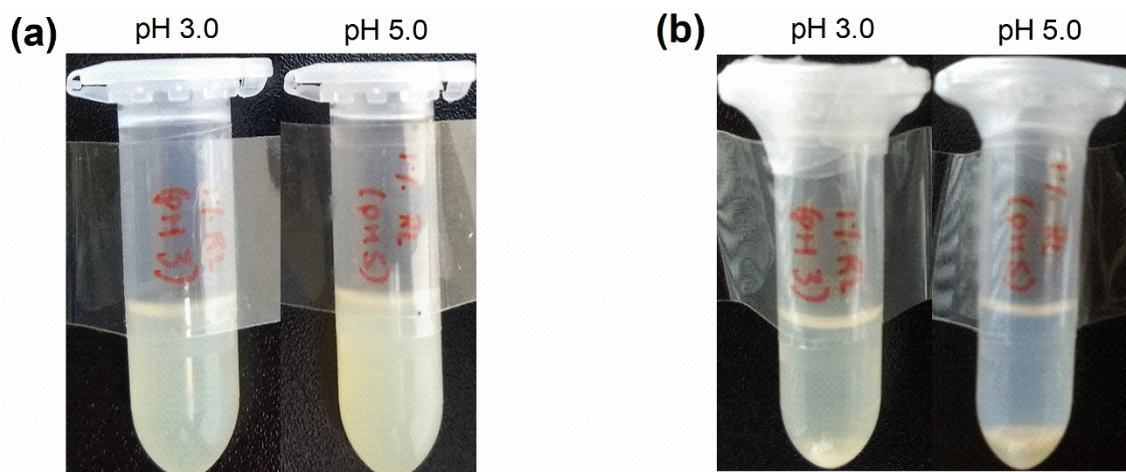
13

14 *Corresponding author: Stefan Salentinig, email: stefan.salentinig@unifr.ch, Tel: +41 26 300

15 8794

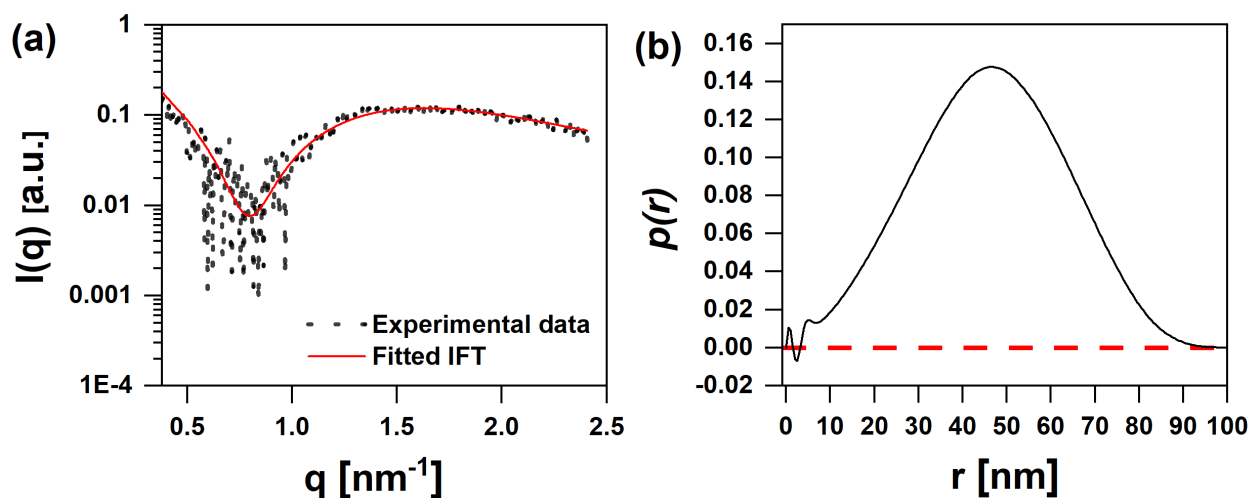
16

1



2 **Figure S1.** Stability of F127-stabilized RL dispersion (a) directly after preparation, and (b)
3 within 30 mins after preparation between pH 3.0-5.0. Formulations with a total lipid
4 concentration of 1% (w/w).

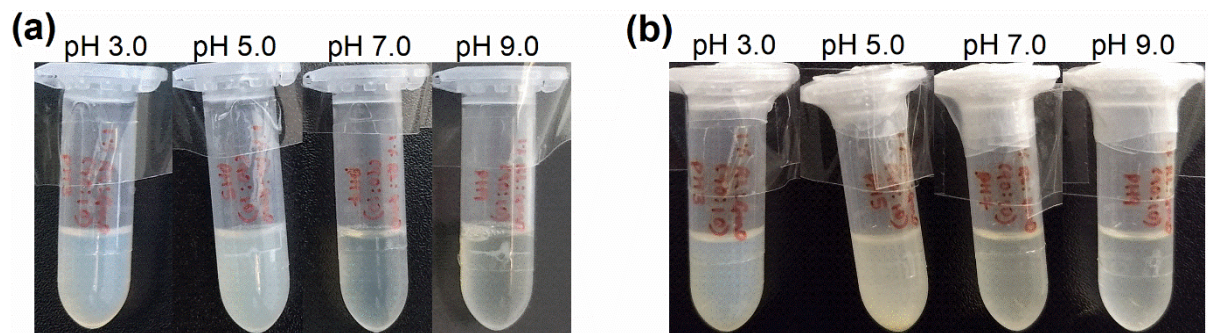
5



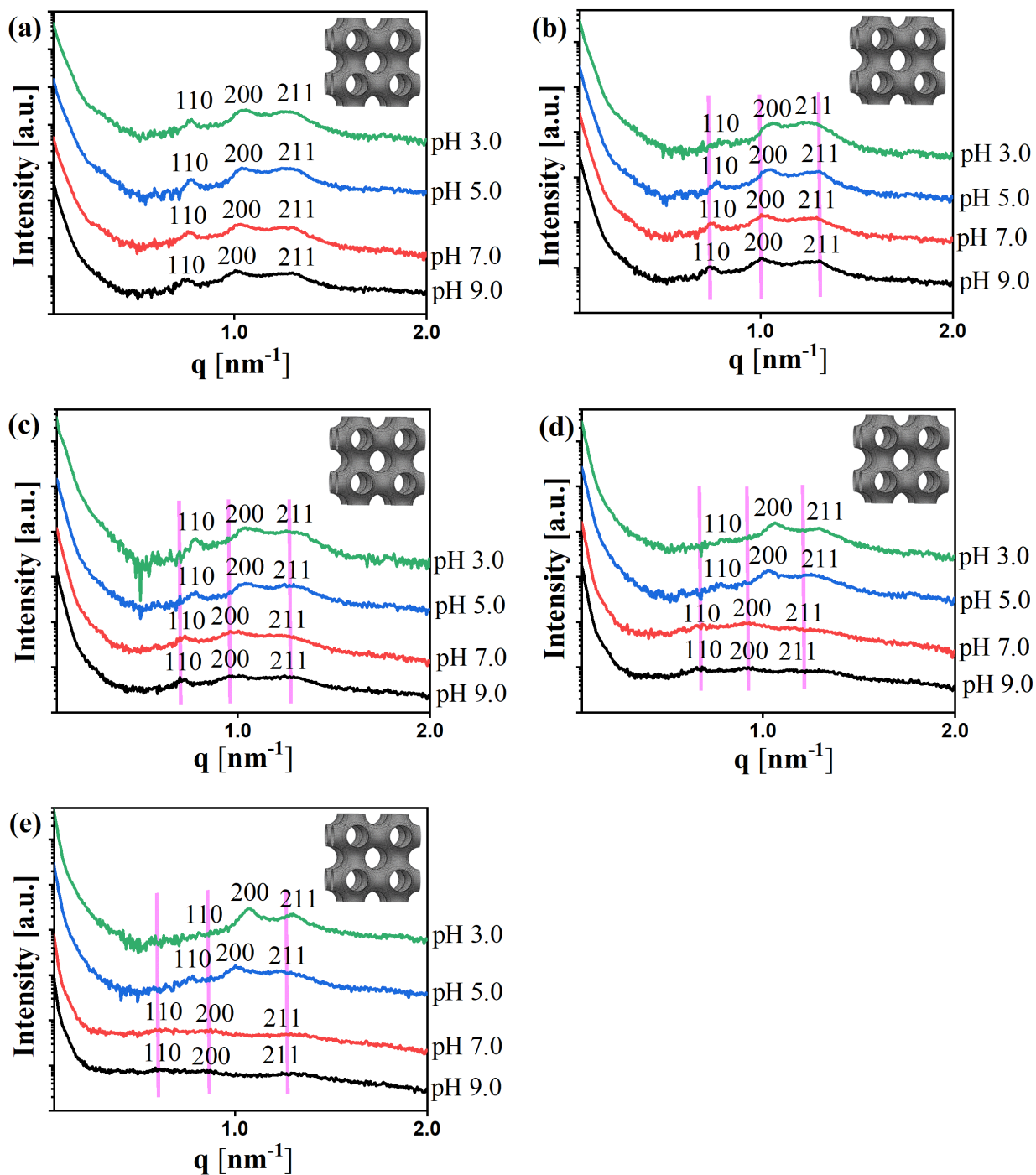
6 **Figure S2.** (a) Experimental SAXS scattering data of RL at pH 7.0 after subtracting the sample
7 background (symbols) and fit calculated with IFT (red curve). (b) The calculated corresponding
8 $p(r)$ for RL at pH 7.0. Oscillations at $r < 10$ nm correspond to the variations in the excess
9 electron density within the bilayer region of RL.

10

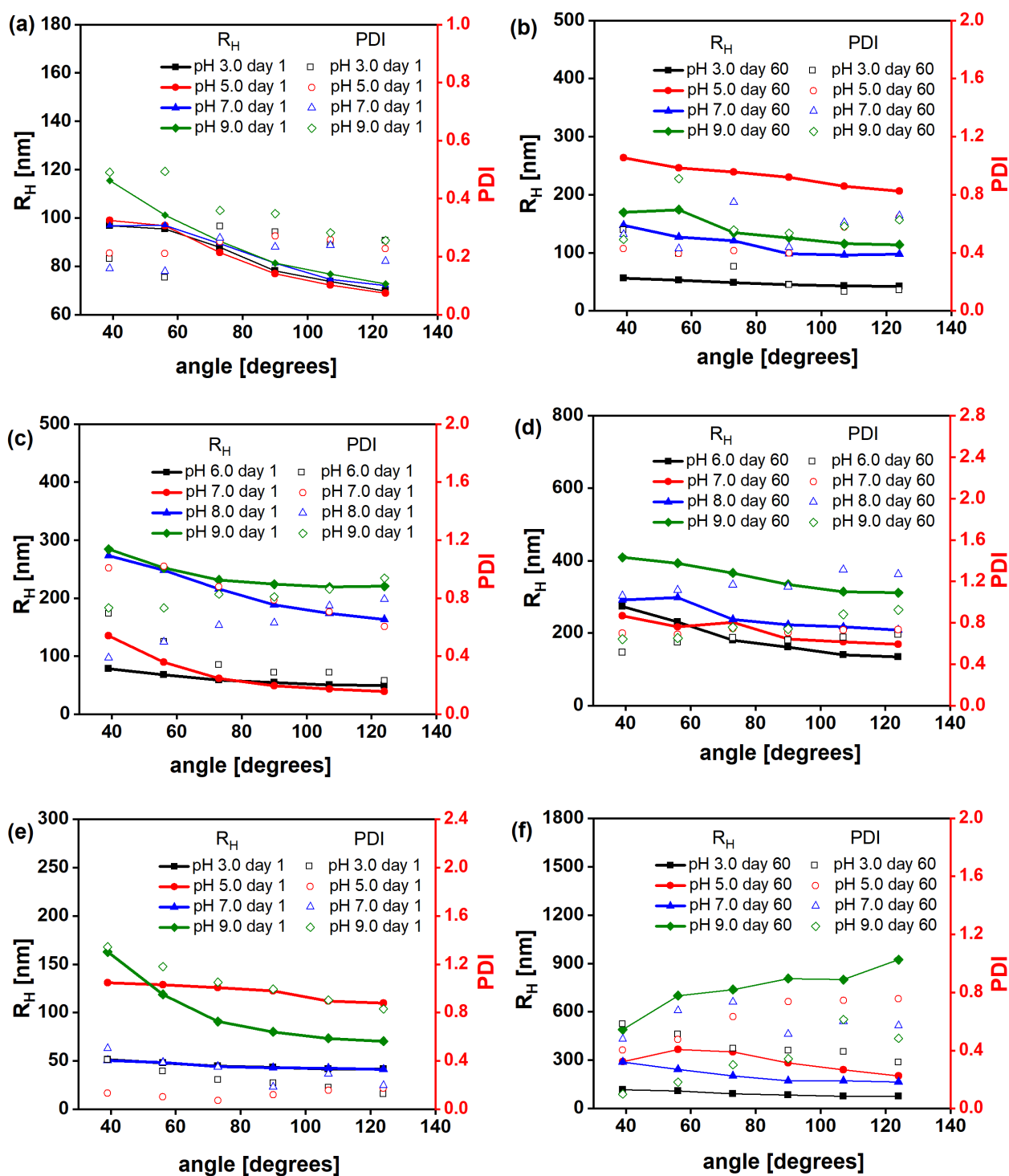
11



1 **Figure S3.** Stability of RL/GMO (90/10 w/w) dispersion (a) directly after preparation, and (b)
2 after 2 months between pH 3.0-9.0. Formulations with a total lipid concentration of 1% (w/w).
3

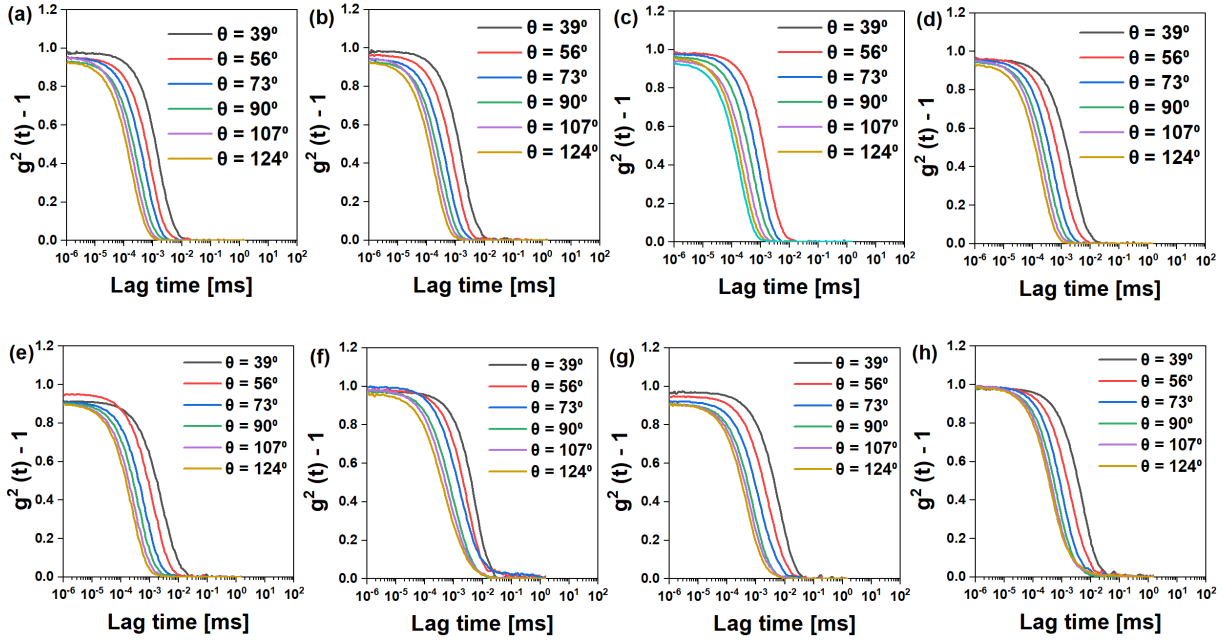


1 **Figure S4.** SAXS curves of (a) RL/GMO = 0/100, (b) RL/GMO = 2/98, (c) RL/GMO = 5/95,
 2 (d) RL/GMO = 10/90, and (e) RL/GMO = 15/85 w/w ratios between pH 3.0-9.0 showing cubic
 3 ($Im\bar{3}m$) structure. The pink line is drawn for visual guidance representing the shift of the Bragg
 4 peaks in the SAXS curves owing to pH-triggered changes in the lattice dimensions (Table S1
 5 and Figure 3 show the corresponding lattice constants).



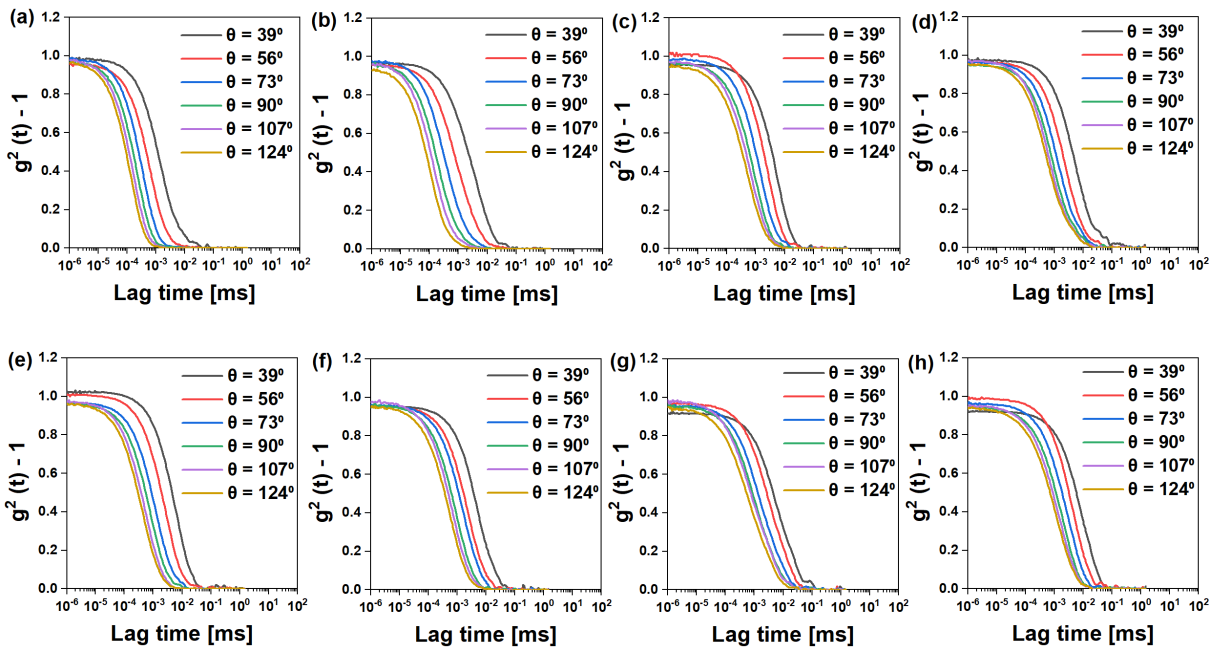
1 **Figure S5.** Summary of the hydrodynamic radius (R_H) and its corresponding PDI value from
2 the multi-angle DLS. (a,b) GMO on day 1 and day 60, respectively between pH 3.0-9.0; (c,d)
3 RL on day 1 and day 60, respectively between pH 6.0-9.0; and (e,f) RL/GMO (90/10 w/w)
4 dispersion on day 1 and day 60, respectively between pH 3.0-9.0. Day 1 refers to measurements
5 conducted directly after preparation.

1



2 **Figure S6.** Intensity correlation functions of GMO dispersion in PBS at scattering angles from
 3 39 to 124° in 17° steps between pH 3.0-9.0. (a) pH 3.0 day 1, (b) pH 5.0 day 1, (c) pH 7.0 day
 4 1, (d) pH 9.0 day 1, (e) pH 3.0 day 60, (f) pH 5.0 day 60, (g) pH 7.0 day 60, and (h) pH 9.0 day
 5 60.

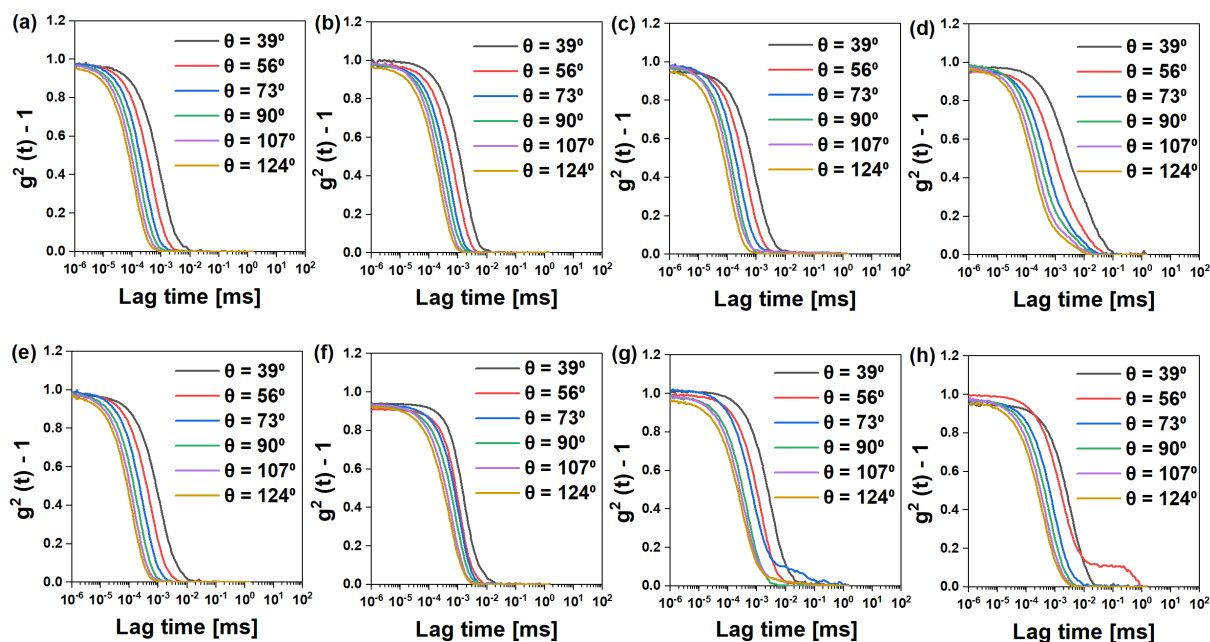
6



7 **Figure S7.** Intensity correlation functions of RL dispersion in PBS at scattering angles from 39
 8 to 124° in 17° steps between pH 6.0-9.0. (a) pH 6.0 day 1, (b) pH 7.0 day 1, (c) pH 8.0 day 1,

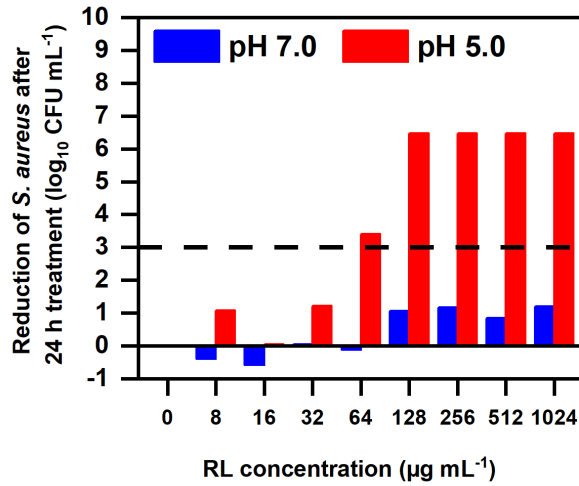
1 (d) pH 9.0 day 1, (e) pH 6.0 day 60, (f) pH 7.0 day 60, (g) pH 8.0 day 60, and (h) pH 9.0 day
2 60.

3

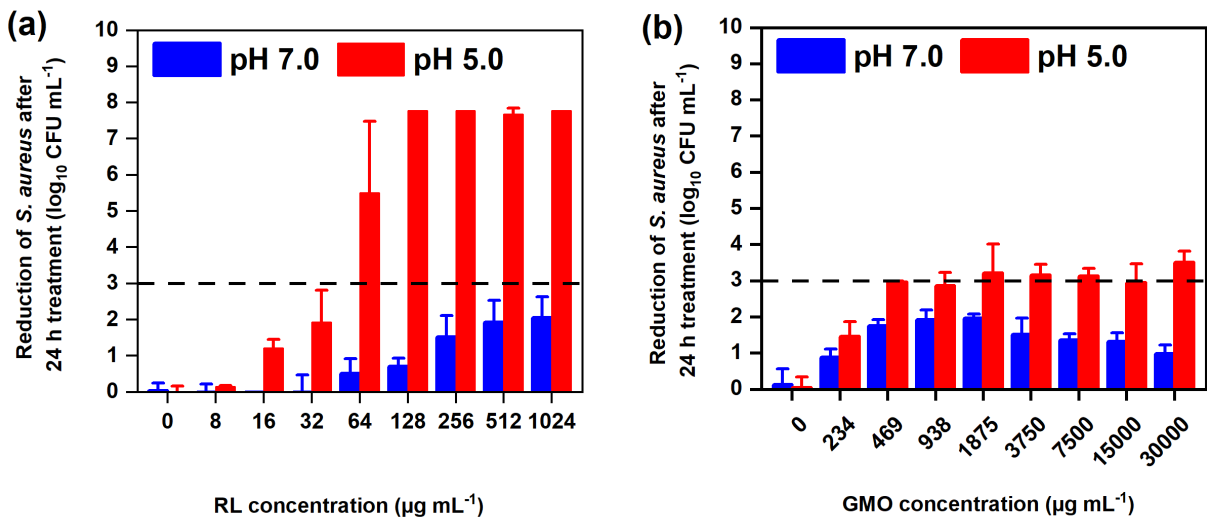


4 **Figure S8.** Intensity correlation functions of RL/GMO (90/10 w/w) dispersion in PBS at
5 scattering angles from 39 to 124° in 17° steps between pH 3.0-9.0. (a) pH 3.0 day 1, (b) pH 5.0
6 day 1, (c) pH 7.0 day 1, (d) pH 9.0 day 1, (e) pH 3.0 day 60, (f) pH 5.0 day 60, (g) pH 7.0 day
7 60, and (h) pH 9.0 day 60.

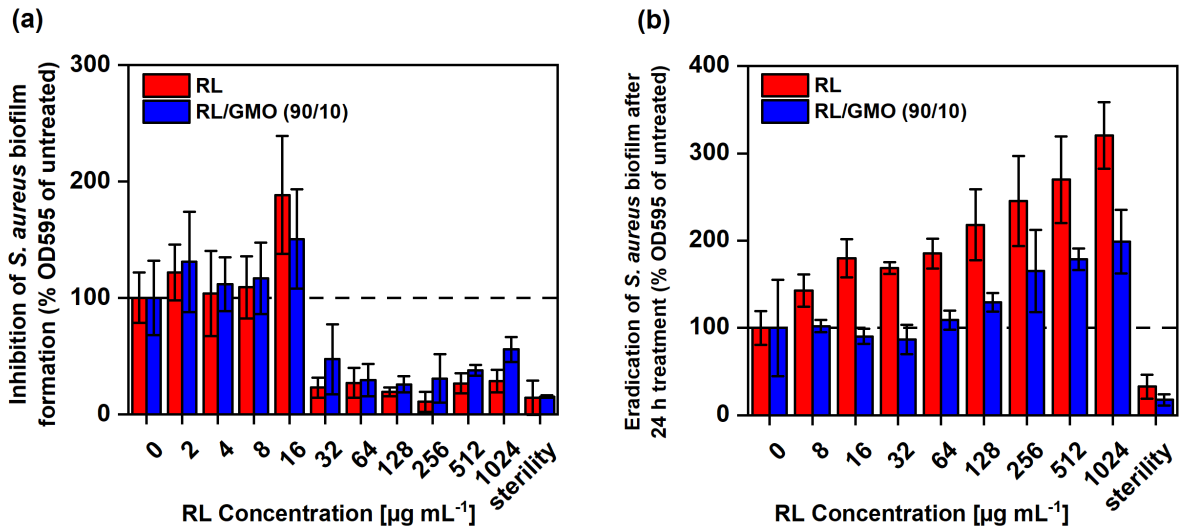
8



1 **Figure S9.** Antibacterial activity of RL/GMO (90/10 w/w) dispersion after two months against
 2 *S. aureus* at pH 5.0 and 7.0, respectively. The dashed line represents the 3-log reduction
 3 threshold, indicating the bactericidal activity (n = 1 with one technical repeat).
 4

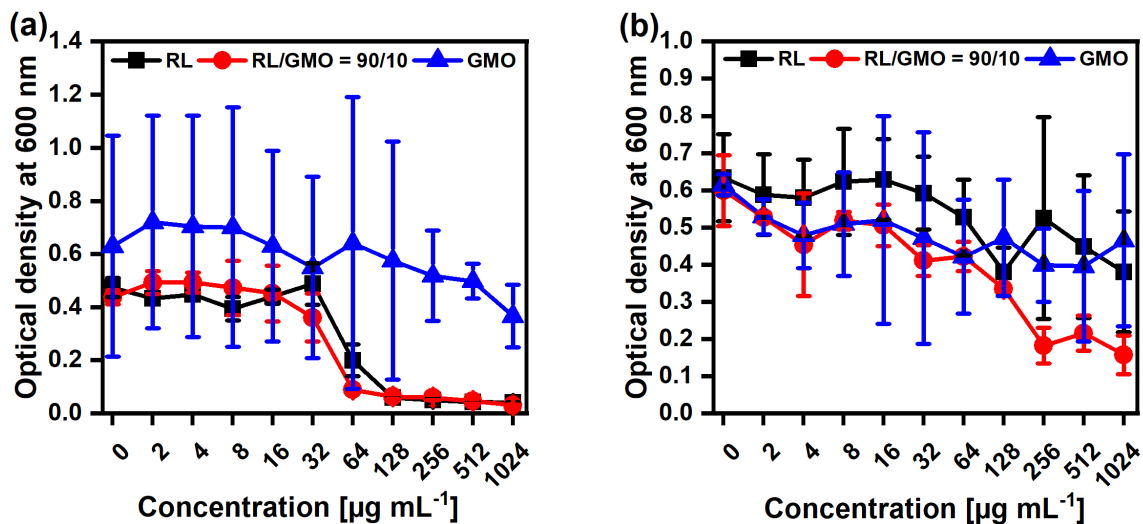


5 **Figure S10.** Antibacterial activity of (a) RL and (b) GMO dispersions against *S. aureus* at pH
 6 5.0 and 7.0, respectively. The dashed line represents the 3-log reduction threshold, indicating
 7 the bactericidal activity (n = 3).
 8



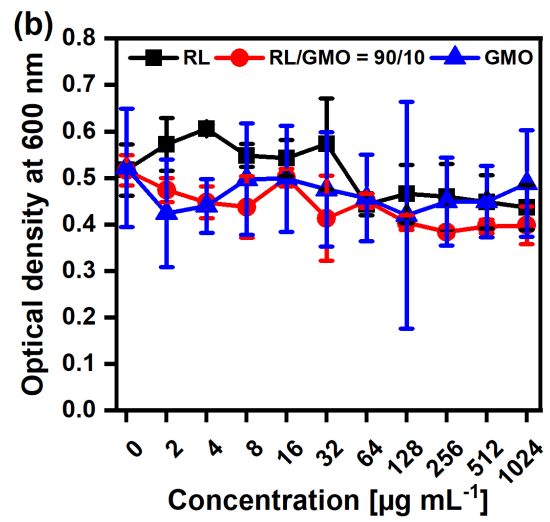
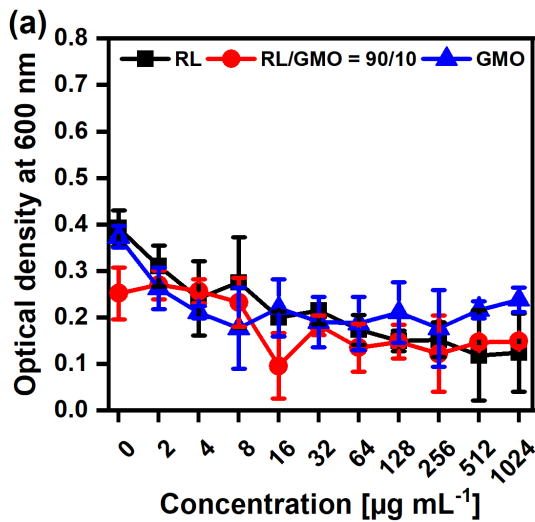
1 **Figure S11.** (a) Inhibition of *S. aureus* biofilm formation by RL/GMO (90/10 w/w) dispersion
 2 at pH 5.0. The biofilm biomass was measured by crystal violet staining after 24 h culture in
 3 RL/GMO dispersion. (b) Eradication of *S. aureus* biofilms by RL/GMO (90/10) dispersion at
 4 pH 5.0. 24 h-old biofilms were treated with RL/GMO dispersion during 24 h and the remaining
 5 biofilm biomass was quantified by crystal violet staining. RL dispersion was used as a positive
 6 control for both assays (n = 3).

7

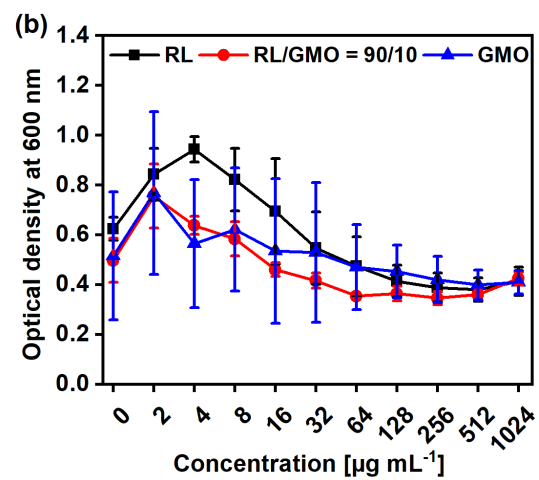
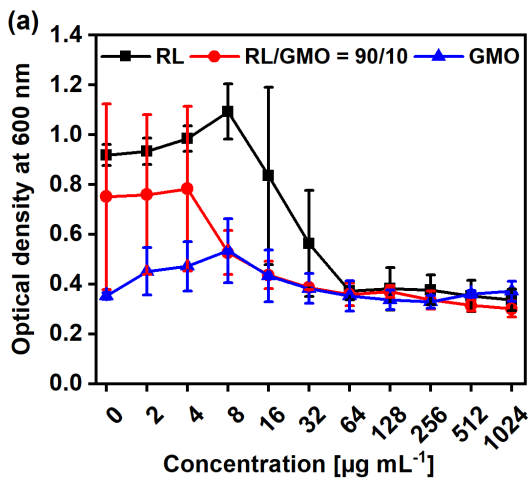


8 **Figure S12.** Antibacterial activity of RL/GMO (90/10 w/w) dispersion against MRSA at (a)
 9 pH 5.0 and (b) pH 7.0. RL and GMO dispersions were used as positive and negative controls,
 10 respectively (n = 3).

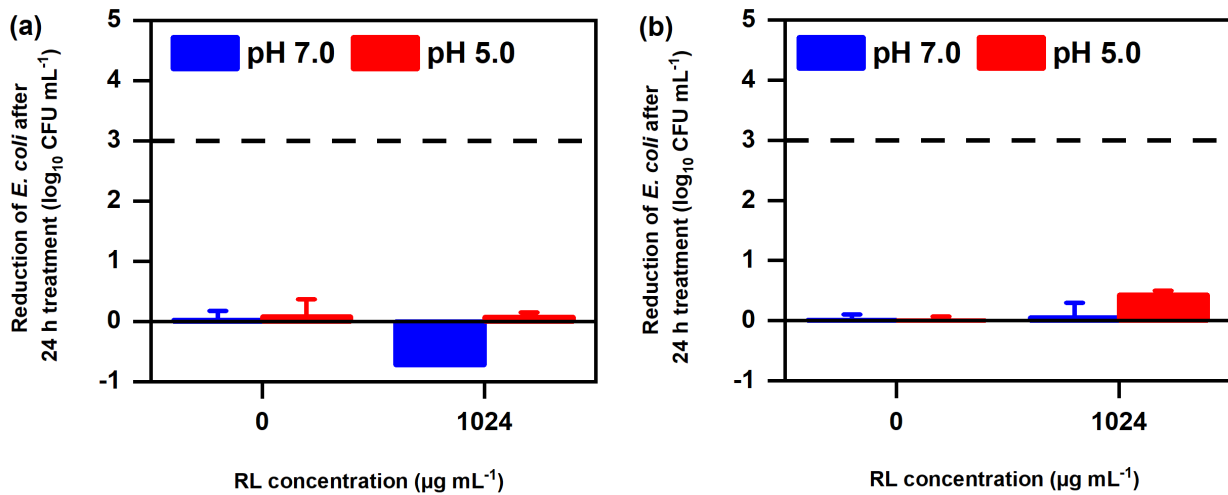
11



1 **Figure S13.** Antibacterial activity of RL/GMO (90/10 w/w) dispersion against *L.*
 2 *monocytogenes* at (a) pH 5.0 and (b) pH 7.0. RL and GMO dispersions were used as positive
 3 and negative controls, respectively (n = 3).
 4

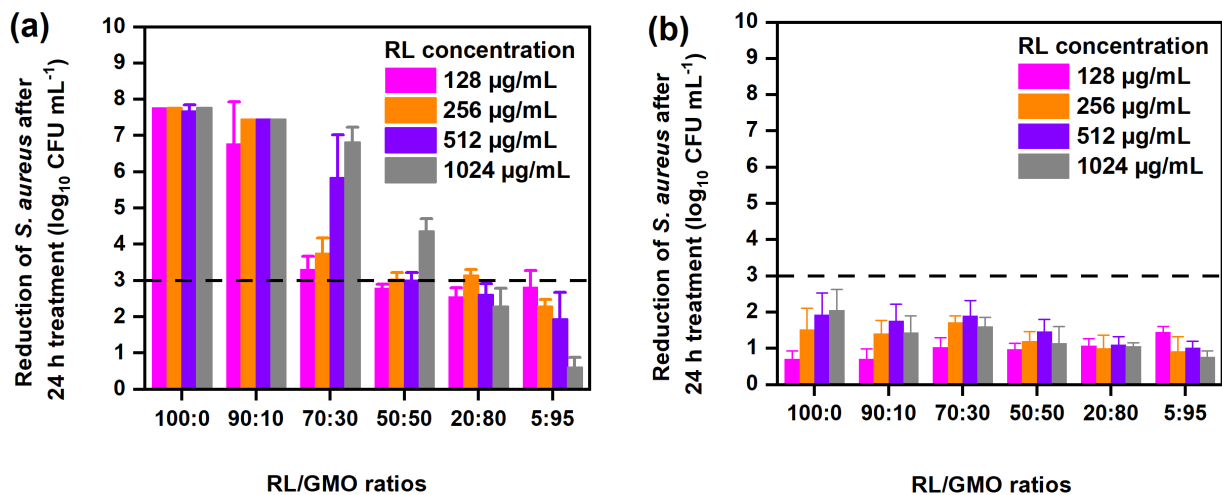


5 **Figure S14.** Antibacterial activity of RL/GMO (90/10 w/w) dispersion against *S. typhimurium*
 6 at (a) pH 5.0 and (b) pH 7.0. RL and GMO dispersions were used as positive and negative
 7 controls, respectively (n = 3).
 8



1 **Figure S15.** Antibacterial activity of (a) RL/GMO (90/10 w/w) and (b) RL dispersions against
 2 *E. coli* at pH 5.0 and 7.0, respectively. The dashed line represents the 3-log reduction threshold,
 3 indicating the bactericidal activity (n = 1 with two technical repeats).

4



5 **Figure S16.** Antibacterial activity of different RL/GMO ratios against *S. aureus* at (a) pH 5.0
 6 and (b) 7.0, respectively. The dashed line represents the 3-log reduction threshold, indicating
 7 the bactericidal activity (n = 3).

8

9

10

11

1 **Table S1.** The calculated average lattice parameter, a_{Im3m} , for the cubic ($Im3m$) structure for
 2 RL/GMO combinations between pH 3.0-9.0.

3

RL/GMO [% w/w]	a_{Im3m} [nm]			
	pH 3.0	pH 5.0	pH 7.0	pH 9.0
0/100	11.7 ± 0.1	11.7 ± 0.1	11.7 ± 0.1	11.7 ± 0.1
2/98	12.1 ± 0.1	12.1 ± 0.1	12.5 ± 0.1	12.8 ± 0.1
5/95	12.2 ± 0.1	12.3 ± 0.1	12.6 ± 0.1	12.8 ± 0.1
10/90	12.0 ± 0.1	12.2 ± 0.1	13.5 ± 0.1	13.6 ± 0.1
15/85	12.1 ± 0.1	12.7 ± 0.1	13.9 ± 0.1	14.0 ± 0.1
20/80	12.1 ± 0.1	12.6 ± 0.1	-	-
25/75	12.1 ± 0.1	12.7 ± 0.1	-	-
30/70	12.0 ± 0.1	12.8 ± 0.1	-	-

4

5

6

7

8

9

10

11

12

13

14

15

16

17

1 **Table S2.** Average R_H and PDI values of different dispersions between pH 3.0-9.0. Day 1
 2 refers to measurements performed after dispersion preparation.

3
 4

GMO								
	pH 3.0		pH 5.0		pH 7.0		pH 9.0	
	Day 1	Day 60						
R_H [nm]	55	74	55	111	55	222	55	111
PDI	0.23	0.44	0.24	0.71	0.20	0.59	0.37	0.60
RL								
	pH 6.0		pH 7.0		pH 8.0		pH 9.0	
	Day 1	Day 60						
R_H [nm]	44	111	32	222	111	222	222	277
PDI	0.39	0.63	0.83	0.72	0.61	1.18	0.82	0.77
RL/GMO (90/10)								
	pH 3.0		pH 5.0		pH 7.0		pH 9.0	
	Day 1	Day 60						
R_H [nm]	37	44	74	222	37	111	55	111
PDI	0.25	0.28	0.12	0.47	0.32	0.57	1.05	0.62

5
 6
 7

8 **Table S3.** MIC values of GMO, RL, and RL/GMO (90/10) against *S. aureus*, MRSA, *L.*
 9 *monocytogenes*, *S. typhimurium*, and *E. coli* at pH 5.0 and pH 7.0. The MIC readout was
 10 impossible due to the dispersed GMO's high optical density indicated by *.

11

MIC [$\mu\text{g mL}^{-1}$] at pH 5.0					
Formulation	<i>S. aureus</i>	MRSA	<i>L. monocytogenes</i>	<i>S. typhimurium</i>	<i>E. coli</i>
GMO	*	*	*	*	*
RL	64	128	> 1024	> 1024	> 1024
RL/GMO (90/10)	64	128	> 1024	> 1024	> 1024
MIC [$\mu\text{g mL}^{-1}$] at pH 7.0					
Formulation	<i>S. aureus</i>	MRSA	<i>L. monocytogenes</i>	<i>S. typhimurium</i>	<i>E. coli</i>
GMO	*	*	*	*	*
RL	> 1024	> 1024	> 1024	> 1024	> 1024
RL/GMO (90/10)	> 1024	> 1024	> 1024	> 1024	> 1024

1